Dorsal premammillary projection to periaqueductal gray controls escape vigor from innate and conditioned threats

Weisheng Wang[1†], Peter J. Schuette[1†], Mimi Q. La-Vu[1], Brooke Christine Tobias[1], Marta Čeko[2], Philip A. Kragel[2,3], Fernando Midea Cuccovia V. Reis[1], Shiyu Ji[1], Megha Sehgal[4], Sandra Maesta-Pereira[1], Meghmik Chakerian[1], Alcino J Silva[1,4], Newton S. Canteras[5], Tor D. Wager[2,6] , Jonathan C. Kao[7], Avishek Adhikari[1,*]

Affiliations

[1] Department of Psychology, University of California, Los Angeles, Los Angeles, CA, 90095, USA.

[2] Institute of Cognitive Science, University of Colorado, Boulder, CO, 80309, USA.

[3] Department of Psychology, Emory University, Atlanta, GA, 30322, USA.

[4] Department of Neurobiology, Department of Psychiatry and Biobehavioral Sciences, University of California, Los Angeles, Los Angeles, CA, 90095, USA.

[5] Department of Anatomy, Institute of Biomedical Sciences, University of São Paulo, São Paulo, SP, 05508-000, Brazil.

[6] Department of Psychological and Brain Sciences, Dartmouth College, NH, 03755, USA.

[7] Department of Electrical and Computer Engineering, University of California, Los Angeles, Los Angeles, CA, 90095, USA.

*Correspondence: avi@psych.ucla.edu

[†]Equal contributions

Abstract

Escape from threats has paramount importance for survival. However, it is unknown if a single circuit controls escape from innate and conditioned threats. The hypothalamic dorsal premammillary nucleus (PMd) may control escape, as it is activated by escape-inducing threats and projects to the region most implicated in flight, the dorsolateral periaqueductal gray (dlPAG). We show that in mice cholecystokinin (cck)-expressing PMd cells are activated during escape, but not other defensive behaviors. PMd-cck ensemble activity can also predict future escape. Furthermore, PMd inhibition decreases escape speed from both innate and conditioned threats. Inhibition of the PMd-cck projection to the dlPAG also decreased escape speed. Lastly, human fMRI data show that a posterior hypothalamic-to-dlPAG pathway increased activity during exposure to aversive images, indicating that a similar pathway may possibly have a related role in humans. Our data identify the PMd as a central node of the escape network.

Introduction

In the presence of life-threatening danger, animals must quickly flee to minimize risk (Perusini and Fanselow, 2015). Due to the vital importance of escape for survival, the neural circuits controlling escape from threats have been extensively studied. The structure studied most commonly in escape is the dorsolateral periaqueductal gray (dlPAG). Stimulation of the dlPAG provokes rapid escape in rodents (Deng et al., 2016; Evans et al., 2018) and panic-related symptoms in humans (Nashold et al.,

1969). Furthermore, single unit dlPAG recordings show that a high proportion of cells are activated during escape (Deng et al., 2016; Evans et al., 2018). In agreement with these data, it has been shown that the dlPAG controls escape vigor, measured by escape velocity (Evans et al., 2018). However, inputs to the dlPAG that may control escape vigor have not been identified. The dorsomedial portion of the ventromedial hypothalamus (VMHdm) is a major excitatory dlPAG input, suggesting that the VMHdm projection may mediate escape. However, activation of the VMHdm projection to the dlPAG surprisingly caused freezing, not escape (Wang et al., 2015). The other main hypothalamic input to the dlPAG is the dorsal premammillary nucleus (PMd) (Canteras and Swanson, 1992; Tovote et al., 2016). Surprisingly, despite being the strongest known input to the panicogenic dlPAG (Canteras and Swanson, 1992; Tovote et al., 2016), the activity of this nucleus has not been directly manipulated or recorded.

The PMd is a key component of the hypothalamic defense system, and is strongly activated by various imminent threats (Cezario et al., 2008). Dangerous stimuli that activate the rodent PMd are extremely diverse, and include carbon dioxide (Johnson et al., 2011), several predators (cats, snakes and ferrets) (Mendes-Gomes et al., 2020) as well as aversive lights and noises (Kim et al., 2017). Additionally, the PMd is also activated by contexts fear conditioned with shocks (Canteras et al., 2008) and social defeat (Faturi et al., 2014), indicating that it may play a role in coordinating defensive behaviors to both innate and conditioned threats. However, to date, the role of the PMd in escape vigor has not been directly studied. Furthermore, escape is generally studied during exposure to innate threats (Deng et al., 2016; Evans et al., 2018). Consequently, it is not known if escape from innate and conditioned threats requires the same circuit. Considering the PMd's involvement in innate and conditioned defense, as explained above, we predicted this region controlled escape from both threat modalities.

Here, we show that cholecystokinin-expressing PMd cells (PMd-cck cells) encoded and predicted escape from innate and conditioned threats. Furthermore, inhibition of these cells or of their projection to the dlPAG decreased escape speed from a live predator or a conditioned threat (a shock grid). Lastly, fMRI data show that a hypothalamic-dlPAG pathway displays increased activation during exposure to aversive images, indicating that a similar pathway from a posterior medial hypothalamic nucleus to the brainstem may also exist in humans. These results show, for the first time, that the PMd is a vital node in coordinating escape from both innate and conditioned threats, and thus is likely to play key roles in minimizing exposure to danger.

Results

Innate and conditioned threats induce defensive behaviors.

To study the PMd's role in controlling defensive behaviors, we exposed mice to two threats: a live predatory rat or a shock grid. These two assays were used to investigate, respectively, innate and conditioned threats. For the rat assay mice were exposed either to a safe control toy rat or an awake rat in a long box (70 cm length, 26 cm width, 44 cm height) for 10 minutes. The rat was placed at one of the corners and its movement was restricted by a harness tied to a wall, restricting its range of motion to the rat area shown in pink in Figure 1A. Rats were screened for low aggression and predatory tendencies and thus they did not attack mice. No separating barrier was used between rats and mice allowing for close naturalistic interactions. Rat and toy rat exposures were separated by 24 hours. For the shock grid assay, mice first explored a different box for 3 consecutive days for 10-minute sessions. The shock grid was placed in one of the corners of the box, as shown in Figure 1A. On day 1, no shocks were given and mice freely explored the environment. On day two, a single 0.7 mA 2 sec shock was given the first time the mouse touched the shock grid. On day 3 (fear retrieval), no shocks were given. All behavioral and neural data plotted from the shock grid is from the fear retrieval day, unless otherwise noted. The pre-shock baseline was used as the control for the fear retrieval day. All sessions were separated by 24 hours (Figure 1B). Threat exposure induced distance from the

threat source, freezing and stretch-attend postures (Figure 1C). Additionally, relative to control assays, during exposure to threat approach velocity was lower while escape velocity was higher (Figure 1C). These results indicate that mice slowly and cautiously approach threats and then escape in high velocity back to safer locations far from threats. Taken together, these data show that both innate and conditioned threats induced defensive behaviors. Our data also support the view that escape velocity is a measure of threat-induced behavior.

Pmd-cck cells are activated by proximity to threat and during escape

We next investigated the activity of PMd cells during threat exposure. To do so, we used a cholecystokinin (cck)-cre line. We then injected AAV-FLEX-GCaMP6s in the PMd and implanted fiberoptic cannula above the injection site in cck-cre mice to record calcium transients in PMd-cck cells using fiber photometry (Figure 2A-B). Averaged heat maps show PMd-cck activity was increased near the rat and the shock grid during fear retrieval (Figure 2C). Indeed, activity was increased near threats relative to control stimuli (toy rat and shock grid in pre-shock day). These comparisons were done when analyzing data at the same speed range (Figure 2D); thus PMd-cck cells are more active near threats independently of locomotor changes. We next studied how PMd-cck cell activity changed during defensive behaviors. A representative trace suggests that these cells show high activity during escape (Figure 2E). Average data show that in both assays PMd-cck cells showed increased activation during risk-assessment stretch-attend postures and during escape, while a decrease in activity was displayed during freezing (Figure 2F-H). Furthermore, the total distance of each escape was correlated with PMd-cck activation during exposure to threats, but not control stimuli (Figure 2I). These results show that PMd-cck cells are quickly activated by proximity to threat and escape, during exposure to both innate and conditioned threats. In agreement with this view, PMd-cck cells displayed relatively high membrane input resistance (484 ± 64 MOhms) and low rheobase, which is the minimum current required to elicit an action potential (38.3 ± 6.1 pA) (Figure 2, figure supplement 1). These results indicate that fairly minor excitatory input is enough to activate these cells. These biophysical characteristics suggest that these cells may be rapidly activated in the presence of threats.

PMd-cck ensemble activity predicts escape occurrence and flight vigor

To analyze how PMd-cck ensemble activity encodes escape, we implanted miniature head mounted fluorescent microscopes (miniscopes) above GCaMP6s-expressing PMd-cck cells (Figure 3A-B). Large ensembles of PMd-cck cells were recorded in the rat and shock grid assays (Figure 3C-D). Using a generalized linear model (GLM), we identified a large fraction of PMd-cck cells that are active during these behaviors (Figure 3E). The behavior that activated the largest and smallest number of PMd-cck cells, was respectively, escape and freezing (Figure 3E). These data agree with our fiber photometry results showing that bulk PMd-cck activity is highest during escape and lowest during freezing. Behavior triggered averages indicate that PMd-cck cells may be significantly activated during defensive behaviors, in agreement with these results (Figure 3F). Further supporting a role for PMd-cck cells in escape, we show that ensemble activity could be used to decode ongoing escape, but not other behaviors (Figure 3G). These intriguing results raise the possibility that PMd-cck activity may be able to predict future occurrence of escape. Indeed, PMd-cck activity could predict escape from innate and conditioned threats several seconds prior to escape onset. However, ensemble activity could not predict movement away from control stimuli (toy rat and shock grid in pre-shock day) (Figure 3H). These data show that PMd-cck activity can specifically predict future escape from threats, but not moving away from objects in general. These data indicate that PMd-cck activity is related to defensive escape, and not to overall locomotion.

Our fiber photometry results indicate that PMd-cck cells were more active during close proximity to threat (Figure 2C). These data suggest that PMd-cck ensemble activity may represent position in threat assays. We thus decoded position in both control and threat assays using PMd-cck ensemble activity. Strikingly, the error of position decoding was smaller in threat than in control assays (Figure

4A-B). These results show that PMd-cck cells represent distance to threat more prominently than distance to control objects.

We then studied if ensemble activity could predict movement vigor, measured by velocity. Indeed, PMd-cck activity could be used to decode velocity during threat exposure with higher accuracy than during exposure to control stimuli (Figure 4, figure supplement 1). Furthermore, decoding of velocity in control assays was less accurate than in threat assays, for both the rat and the shock assays (Figure 4. Figure supplement 1). Since PMd ensemble activity can predict future escape, but not approach, we hypothesized that PMd activity could be used to decode velocity away from threats more accurately than velocity towards threats. Representative traces showing predicted and observed velocity support this hypothesis (Figure 4C). Indeed, averaged data across mice show that the error for predicted velocity is lower for decoding velocity away from threat compared to velocity towards threat (Figure 4C-D). These data show that PMd-cck cells represent key kinematic variables related to rapid escape from threats.

PMd-cck inhibition decreases escape vigor

Recordings of PMd-cck ensemble activity revealed that these cells are highly active during escape and that their activity can be used to decode escape (but not approach) velocity. Moreover, neural activity could only decode escape, but not other behaviors. We thus hypothesized that inhibition of PMd-cck cells would decrease escape velocity without affecting other defensive behaviors. To test this view, we expressed the inhibitory receptor hM4Di in PMd-cck cells (Figure 5A). We confirmed that the hM4Di receptor ligand clozapine-n-oxide produced hyperpolarization (Figure 5B). We then exposed mice to the assays described in Figure 1A. Mice were exposed to each threat and control assay twice, following treatment with either saline or the hM4Di ligand clozapine-N-oxide (CNO) (Figure 5C). Inhibition of PMd-cck cells in CNO-treated mice decreased escape velocity from both threats, in line with our prediction (Figure 5D). Importantly, inhibiting these cells did not change velocity while mice moved away from control safe stimuli (toy rat and shock grid prior to fear conditioning) (Figure 5, figure supplement 1). This manipulation did not change freezing or stretch-attend postures (Figure 5D), showing PMd-cck activity is selectively required for escape, rather than defensive behaviors in general.

Activation of PMd-cck cells recruits a wide network of regions involved in defensive behaviors

As PMd-cck inhibition decreases escape velocity, but not other behaviors, we predicted that activating these cells would specifically induce running and escape-related motion. Indeed, optogenetic activation of ChR2-expressing PMd-cck cells caused an increase in speed, but not in the amount of freezing or stretch-attend postures (Figure 6A-B).

We next investigated which downstream regions are recruited following activation of PMd-cck cells. Prior studies showed that the PMd projects to several structures involved in defense, such as the dorsolateral periaqueductal gray (dlPAG) and the anterior hypothalamus. Interestingly, it also projects to the anteromedial ventral thalamus (amv) (Canteras and Swanson, 1992). The amv has head direction cells (Bassett et al., 2007) and is a region critical for spatial navigation (Jankowski et al., 2013) and threat-conditioned contextual memory (Carvalho-Netto et al., 2010).

We hypothesized that activation of PMd-cck cells would recruit not only these known direct downstream areas, but also other structures involved in mounting a defensive behavioral state and regions involved in escape-related motor actions. To test this hypothesis we optogenetically activated ChR2-expressing PMd-cck cells with blue light for 10 minutes (20 Hz, 5 ms pulses). Following perfusion, we performed an antibody stain against the immediate early gene cfos. PMd activation

increased fos expression in regions that it projects to, such as the amv and the dlPAG. Interestingly, other nuclei critical for defensive behaviors, such as the basolateral amygdala, lateral septum and the bed nucleus of the stria terminalis were also activated (Figure 6C), even though they are not innervated by the PMd (Canteras and Swanson, 1992). These results show that the PMd recruits not only its direct downstream outputs, but also other regions involved in threat-related defense. Striatal regions were also activated, such as the caudate nucleus, possibly due to the hyperlocomotion and escape-related actions observed during optogenetic stimulation. Importantly, not all regions were engaged, showing functional specificity. For example, the dentate gyrus and the PMd-adjacent ventral premammillary nucleus did not show increases in fos expression following PMd stimulation (Figure 6D). These data show that PMd-cck cells can recruit a broad network of threat-activated regions, which may contribute to a transition to a defensive state.

The dorsolateral periaqueductal gray (dlPAG) is active during escape

To identify which PMd downstream targets controlled escape, we studied its two main outputs, the anteromedial ventral thalamus (amv) and the dorsolateral periaqueductal gray (dlPAG) (Canteras and Swanson, 1992). The amv has head direction cells (Bassett et al., 2007) and is a region critical for threat-conditioned contextual memory (Carvalho-Netto et al., 2010) and spatial navigation (Jankowski et al., 2013).

The amv is also necessary for the acquisition of contextual fear elicited by predators (Carvalho-Netto et al., 2010), demonstrating this region has a role in defensive behaviors. In contrast, the dlPAG is a critical node in the escape network (Del-Ben and Graeff, 2009; Tovote et al., 2016).

To identify which of these PMd outputs control escape speed, we injected AAV9-syn-GCaMP6s in wild type mice in either the amv or the dlPAG and obtained calcium transient recordings in the rat and shock grid assays (Figure 7A). DLPAG activity increased during escape from the rat (Figure 7C), in agreement with prior work showing this region is active during escape from innate threats (Deng et al., 2016; Evans et al., 2018). However, the dlPAG also showed increased activity during exposure to the fear conditioned shock grid during fear retrieval (Figure 7D-E). To our knowledge, there are no prior reports showing the dlPAG is active during escape from conditioned threats. Surprisingly, like the dlPAG, the amv was also active during escape from both threat modalities (Figure 7G-I), even though there are no prior reports implicating the amv in escape.

Inhibition of the PMd-cck projection to the dlPAG decreases escape speed

Our fiber photometry results show that both major outputs of the PMd to the dlPAG and the amv are active during escape from threats, indicating the PMd-cck projections to these regions may control escape vigor. To identify which projection controlled escape vigor, we expressed the inhibitory opsin Arch in PMd-cck cells and implanted fiberoptic cannulae bilaterally over either the amv or the dlPAG (Figure 8A-C). Inhibition of the PMd-cck projection to the dlPAG with green light decreased escape velocity in both assays (Figure 8D). This manipulation did not alter other defensive behaviors such as freezing or stretch-attend postures (Figure 8D). In contrast, inhibition of the PMd-cck projection to the amv did not change any defensive behavioral measure in either assay (Figure 8E). These data show that the activity in the PMd-cck projection to the dlPAG, but not to the amv, is necessary for normal escape vigor during exposure to both innate and conditioned threats.

Hypothalamic-PAG functional connectivity increases in humans viewing aversive images

To investigate whether a functionally similar pathway exists in humans, we examined functional connectivity (i.e., covariation of BOLD signal in the hypothalamus and PAG) as participants received aversive stimulation during fMRI scanning (N = 48). We developed a predictive model to identify a pathway between the hypothalamus (HTH) and the PAG, which consisted of a multi-voxel pattern across brain voxels in each region optimized for maximal HTH-PAG covariation (Figure 9, see

Methods). We then tested activation in this pathway in held-out participants. This HTH-PAG pathway responded more strongly to aversive images than non-aversive images and its activation also scaled monotonically with aversiveness (Figure 9C). Examination of the multi-voxel patterns contributing to the HTH-PAG pathway revealed that portions of medial posterior hypothalamus (neighboring the mammillary bodies) were most consistently associated with PAG activation. We also show that activation of the HTH-PAG pathway is selective and does not correlate with activation of a different major subcortical input pathway to the PAG, such as the amygdala-PAG pathway (Figure 9, figure supplement 1).

Thus, these data show that functional connectivity in a hypothalamic-PAG pathway is increased in humans during aversive situations, in agreement with our results in mice showing that the hypothalamic to brainstem PMd-dlPAG pathway is engaged during escape from aversive threats.

Discussion

The PMd is anatomically the source of the most prominent input to the dlPAG (Del-Ben and Graeff, 2009; Lovick, 2000; Tovote et al., 2016). A wealth of evidence from diverse streams of data have demonstrated that the dlPAG controls escape (Del-Ben and Graeff, 2009; Tovote et al., 2016). Recent work has also shown that the dlPAG controls escape vigor (Evans et al., 2018). Taken together, these data indicate that the PMd is anatomically well-situated to modulate escape vigor from threats. Furthermore, optogenetic activation of PMd-cck cells activates a broad network of regions involved in defensive behaviors (Figure 6D). Our fos data show PMd-cck cell optogenetic activation recruited a plethora of areas known to mediate defense, such as the basolateral amygdala, the lateral septum and the bed nucleus of the stria terminalis. These results indicate that PMd-activation potentially may affect a wide range of defensive behaviors by engaging these networks.

Our data provide strong evidence showing PMd-cck cells play a key role in controlling escape vigor, measured by velocity. First, PMd-cck cells were activated by threat proximity (Figure 2D and 4B), their activity predicted future escape (Figure 3H) and represented escape velocity, but not approach velocity (Figure 4D). Second, inhibition of either PMd-cck cells (Figure 5) and of the PMd-cck to dlPAG inhibition decreased escape velocity (Figure 7). These data demonstrate the PMd-cck projection to the dlPAG is critical for modulating escape velocity from threats, which is a behavior of paramount importance for survival.

Interestingly, our data show that the PMd, as well as the dlPAG participate in defensive responses elicited by both innate and shock-based conditioned threats. The dlPAG has mostly been studied as a region that initiates escape from innate threats, such as looming stimuli (Evans et al., 2018). However, prior evidence has also implicated the dlPAG in conditioned defensive behavior. For example, the dlPAG is activated during exposure to shock-conditioned auditory tones and contexts (Carrive et al., 1997; Watson et al., 2016). Furthermore, neurotransmission of cannabinoids (Resstel et al., 2008), CRF (Borelli et al., 2013), glutamate and nitric oxide (Aguiar et al., 2014) have been shown to be necessary for contextual freezing. However, involvement of the dlPAG or the PMd in escape from conditioned stimuli such as shock grids is less well-understood.

We now show that the PMd-cck projection to the dlPAG modulates escape velocity from conditioned threats, broadening the role of this circuit to include escape from learned threats. The dlPAG is bidirectionally connected with diverse forebrain regions (Motta et al., 2017), while the PMd receives strong input from the medial prefrontal cortex (Comoli et al., 2000), which may explain how these regions respond to conditioned threats. Intriguingly, during contextual fear retrieval tests, rats showed increased PMd fos expression if they had free access to the conditioning chamber, but not if

they were confined to this chamber (Viellard et al., 2016). Information about innate predatory threats are likely conveyed to the PMd by other members of the hypothalamic predatory defense circuit, such as the VMHdm and the anterior hypothalamus (Cezario et al., 2008; Comoli et al., 2000; Silva et al., 2013). Future studies are needed to determine which specific inputs to the PMd convey information about conditioned threats. Nevertheless, our data show that the PMd-dlPAG circuit is not merely responding to external threatening sensory cues. Rather, the involvement of this circuit in escape from conditioned stimuli during fear retrieval shows that these structures can be affected by long-term fear memories, illustrating that evolutionarily ancient structures can also display experience-dependent roles in behavior.

The amv was activated during escape (Figure 7), inhibition of the PMd-cck projection to the amv did not alter escape, freeze or stretch risk-assessment postures (Figure 8D). These data indicate that the amv's role in defensive behavior may be related to contextual memory-associated behaviors rather than the execution of escape or freezing (Carvalho-Netto et al., 2010).

Intriguingly, our fMRI data indicate that a hypothalamic-PAG pathway has increased activity in humans viewing aversive images (Figure 9). A homologous functional pathway to the rodent PMd-dlPAG may exist in humans, that is at least partially identifiable from fMRI data. We used a novel application of Partial Least Squares to identify local multi-voxel patterns that functionally connected HTH and dlPAG. In out-of-sample tests in new participants, HTH and dlPAG were positively correlated in every participant and tracked the reported intensity of negative emotion elicited by images. The resolution of imaging in humans does not allow us to specify which hypothalamic nucleus is involved. However, the location of the nucleus is in the posterior medial hypothalamus, similar to the rodent PMd, suggesting the possibility that a circuit analogous to the PMd-dlPAG projection may exist in humans. It is not feasible to directly study functional connectivity in humans during actual escape from threats, so we were limited to collecting data during exposure to aversive images. Despite these limitations, these data are compatible with rodent data showing the PMd is activated by a wide variety of aversive stimuli such as bright lights and loud noises (Kim et al., 2017).

Taken together, our data indicate that the PMd-cck projection to the dlPAG modulates escape velocity during exposure to both innate and conditioned threats, and the results suggest a similar pathway may be active during exposure to aversive situations in humans.

Acknowledgements

We were supported by the NIMH (R00 MH106649 and R01 MH119089) (A.A.), the Brain and Behavior Research Foundation (Grants # 22663, 27654, 27780 and 29204 respectively to A.A, F.M.C.V.R, W.W and J.C.K.), the NSF (NSF-GRFP DGE-1650604, P.J.S), the UCLA Affiliates fellowship (P.J.S.) the Achievements Rewards for College Scientists Foundation and NIMH F31 MH121050-01A1(M.Q.L) and the Hellman Foundation (A.A.). FAPESP, Research Grant #2014/05432-9, (N.S.C.). F.M.C.V.R. was supported with FAPESP grants #2015/23092-3 and #2017/08668-1.

Competing interests

The authors declare no competing interests.

References

Adhikari A, Lerner TN, Finkelstein J, Pak S, Jennings JH, Davidson TJ, Ferenczi E, Gunaydin LA, Mirzabekov JJ, Ye L, Kim S-Y, Lei A, Deisseroth K. Aharoni D, Hoogland TM. 2015. Basomedial amygdala mediates top-down control of anxiety and fear. Nature **527**:179–185.

Aharoni D, Hoogland TM. 2019. Circuit Investigations With Open-Source Miniaturized Microscopes: Past, Present and Future. *Front Cell Neurosci* **13**:141.

Bassett JP, Tullman ML, Taube JS. 2007. Lesions of the tegmentomammillary circuit in the head direction system disrupt the head direction signal in the anterior thalamus. *J Neurosci* **27**:7564–7577.

Borelli KG, Albrechet-Souza L, Fedoce AG, Fabri DS, Resstel LB, Brandão ML. 2013. Conditioned fear is modulated by CRF mechanisms in the periaqueductal gray columns. *Horm Behav* **63**:791–799.

Cai DJ, Aharoni D, Shuman T, Shobe J, Biane J, Song W, Wei B, Veshkini M, La-Vu M, Lou J, Flores SE, Kim I, Sano Y, Zhou M, Baumgaertel K, Lavi A, Kamata M, Tuszynski M, Mayford M, Golshani P, Silva AJ. 2016. A shared neural ensemble links distinct contextual memories encoded close in time. *Nature* **534**:115–118.

Canteras NS, Kroon JAV, Do-Monte FHM, Pavesi E, Carobrez AP. 2008. Sensing danger through the olfactory system: the role of the hypothalamic dorsal premammillary nucleus. *Neurosci Biobehav Rev* **32**:1228–1235.

Canteras NS, Swanson LW. 1992. The dorsal premammillary nucleus: an unusual component of the mammillary body. *Proc Natl Acad Sci U S A* **89**:10089–10093.

Carrive P, Leung P, Harris J, Paxinos G. 1997. Conditioned fear to context is associated with increased Fos expression in the caudal ventrolateral region of the midbrain periaqueductal gray. *Neuroscience* **78**:165–177.

Carvalho-Netto EF, Martinez RCR, Baldo MVC, Canteras NS. 2010. Evidence for the thalamic targets of the medial hypothalamic defensive system mediating emotional memory to predatory threats. *Neurobiol Learn Mem* **93**:479–486.

Cezario AF, Ribeiro-Barbosa ER, Baldo MVC, Canteras NS. 2008. Hypothalamic sites responding to predator threats--the role of the dorsal premammillary nucleus in unconditioned and conditioned antipredatory defensive behavior. *Eur J Neurosci* **28**:1003–1015.

Comoli E, Ribeiro-Barbosa ÉR, Canteras NS. 2000. Afferent connections of the dorsal premammillary nucleus. *J Comp Neurol* **423**:83–98.

Del-Ben CM, Graeff FG. 2009. Panic Disorder: Is the PAG Involved? *Neural Plasticity*. doi:10.1155/2009/108135

Deng H, Xiao X, Wang Z. 2016. Periaqueductal Gray Neuronal Activities Underlie Different Aspects of Defensive Behaviors. *J Neurosci* **36**:7580–7588.

Evans DA, Vanessa Stempel A, Vale R, Ruehle S, Lefler Y, Branco T. 2018. A synaptic threshold mechanism for computing escape decisions. *Nature*. doi:10.1038/s41586-018-0244-6

Faturi CB, Rangel MJ Jr, Baldo MVC, Canteras NS. 2014. Functional mapping of the circuits involved in the expression of contextual fear responses in socially defeated animals. *Brain Struct Funct* **219**:931–946.

Hardoon DR, Szedmak S, Shawe-Taylor J. 2004. Canonical correlation analysis: an overview with application to learning methods. *Neural Comput* **16**:2639–2664.

Haxby JV, Guntupalli JS, Connolly AC, Halchenko YO, Conroy BR, Gobbini MI, Hanke M, Ramadge PJ. 2011. A common, high-dimensional model of the representational space in human ventral temporal cortex. *Neuron* **72**:404–416.

Jankowski MM, Ronnqvist KC, Tsanov M, Vann SD, Wright NF, Erichsen JT, Aggleton JP, O'Mara SM. 2013. The anterior thalamus provides a subcortical circuit supporting memory and spatial navigation. *Frontiers in Systems Neuroscience*. doi:10.3389/fnsys.2013.00045

Kim CK, Yang SJ, Pichamoorthy N, Young NP, Kauvar I, Jennings JH, Lerner TN, Berndt A, Lee SY, Ramakrishnan C, Davidson TJ, Inoue M, Bito H, Deisseroth K. 2016. Simultaneous fast measurement of circuit dynamics at multiple sites across the mammalian brain. *Nat Methods* **13**:325–328.

Kim DJ, Lee AS, Yttredahl AA, Gómez-Rodríguez R, Anderson BJ. 2017. Repeated threat (without direct harm) alters metabolic capacity in select regions that drive defensive behavior. *Neuroscience* **353**:106–118.

Kim EJ, Horovitz O, Pellman BA, Tan LM, Li Q, Richter-Levin G, Kim JJ. 2013. Dorsal periaqueductal gray-amygdala pathway conveys both innate and learned fear responses in rats. *Proc Natl Acad Sci U S A* **110**:14795–14800.

Kragel PA, Bianciardi M, Hartley L, Matthewson G, Choi J-K, Quigley KS, Wald LL, Wager TD, Feldman Barrett L, Satpute AB. 2019. Functional Involvement of Human Periaqueductal Gray and Other Midbrain Nuclei in Cognitive Control. *J Neurosci* **39**:6180–6189.

Lang PJ, Bradley MM, Cuthbert BN. 2008. International affective picture system (IAPS): affective ratings of pictures and instruction manual. University of Florida, Gainesville. Tech Rep A-8.

Lovick TA. 2000. Panic Disorder-A Malfunction of Multiple Transmitter Control Systems within the Midbrain Periaqueductal Gray Matter? *Neuroscientist* **6**:48–59.

Mendes-Gomes J, Motta SC, Passoni Bindi R, de Oliveira AR, Ullah F, Baldo MVC, Coimbra NC, Canteras NS, Blanchard DC. 2020. Defensive behaviors and brain regional activation changes in rats confronting a snake. *Behav Brain Res* **381**:112469.

Motta SC, Carobrez AP, Canteras NS. 2017. The periaqueductal gray and primal emotional processing critical to influence complex defensive responses, fear learning and reward seeking. *Neurosci Biobehav Rev* **76**:39–47.

Nagai J, Rajbhandari AK, Gangwani MR, Hachisuka A, Coppola G, Masmanidis SC, Fanselow MS, Khakh BS. 2019. Hyperactivity with Disrupted Attention by Activation of an Astrocyte Synaptogenic Cue. *Cell* **177**:1280–1292.e20.

Nath T, Mathis A, Chen AC, Patel A, Bethge M, Mathis MW. 2019. Using DeepLabCut for 3D markerless pose estimation across species and behaviors. *Nat Protoc* **14**:2152–2176.

Pauli WM, Nili AN, Tyszka JM. 2018. A high-resolution probabilistic in vivo atlas of human subcortical brain nuclei. *Sci Data* **5**:180063.

Perusini JN, Fanselow MS. 2015. Neurobehavioral perspectives on the distinction between fear and anxiety. *Learn Mem* **22**:417–425.

Resstel LBM, Lisboa SF, Aguiar DC, Corrêa FMA, Guimarães FS. 2008. Activation of CB1 cannabinoid receptors in the dorsolateral periaqueductal gray reduces the expression of contextual fear conditioning in rats. *Psychopharmacology* **198**:405–411.

Schuette PJ, Reis FMCV, Maesta-Pereira S, Chakerian M, Torossian A, Blair GJ, Wang W, Blair HT, Fanselow MS, Kao JC, Adhikari A. 2020. Long-Term Characterization of Hippocampal Remapping during Contextual Fear Acquisition and Extinction. *J Neurosci* **40**:8329–8342.

Silva BA, Mattucci C, Krzywkowski P, Murana E, Illarionova A, Grinevich V, Canteras NS, Ragozzino D, Gross CT. 2013. Independent hypothalamic circuits for social and predator fear. *Nat Neurosci* **16**:1731–1733.

Tovote P, Esposito MS, Botta P, Chaudun F, Fadok JP, Markovic M, Wolff SBE, Ramakrishnan C, Fenno L, Deisseroth K, Herry C, Arber S, Lüthi A. 2016. Midbrain circuits for defensive behaviour. *Nature*

534:206–212.

Viellard J, Baldo MV, Canteras NS. 2016. Testing conditions in shock-based contextual fear conditioning influence both the behavioral responses and the activation of circuits potentially involved in contextual avoidance. *Behav Brain Res.* **315:** 123-129

Wang L, Chen IZ, Lin D. 2015. Collateral pathways from the ventromedial hypothalamus mediate defensive behaviors. *Neuron* **85**:1344–1358.

Watson TC, Cerminara NL, Lumb BM, Apps R. 2016. Neural Correlates of Fear in the Periaqueductal Gray. *J Neurosci* **36**:12707–12719.

Wold S, Sjöström M, Eriksson L. 2001. PLS-regression: a basic tool of chemometrics. *Chemometrics Intellig Lab Syst* **58**:109–130.

Zhou P, Resendez SL, Rodriguez-Romaguera J, Jimenez JC, Neufeld SQ, Giovannucci A, Friedrich J, Pnevmatikakis EA, Stuber GD, Hen R, Kheirbek MA, Sabatini BL, Kass RE, Paninski L. 2018. Efficient and accurate extraction of in vivo calcium signals from microendoscopic video data. *Elife* **7**. doi:10.7554/eLife.28728

Figures

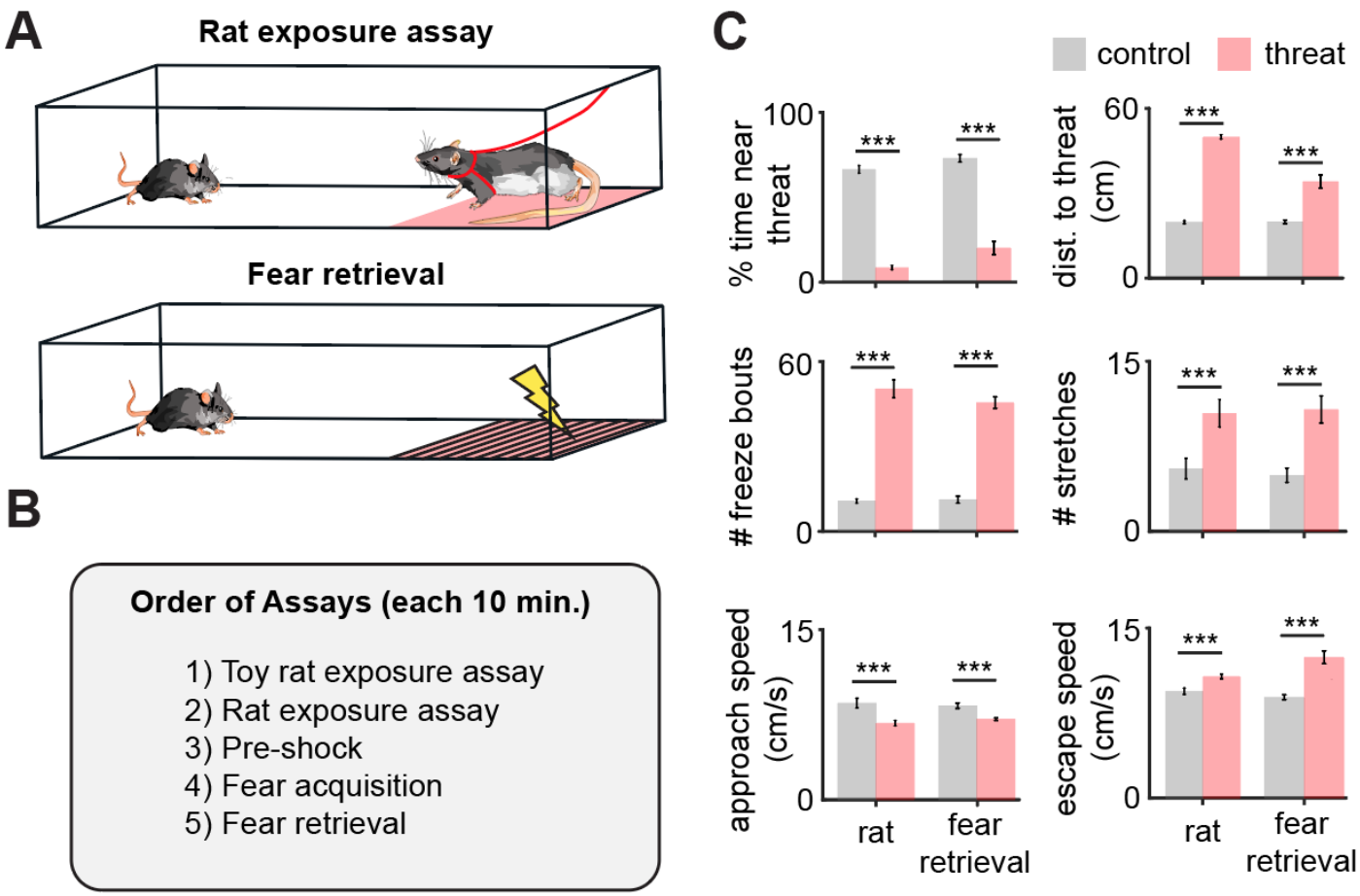

Figure 1. Rat and fear retrieval assays increased fear-related metrics. (**A**) Schemes of (top) rat assay and (bottom) fear retrieval assay. The rat is restricted by a harness (shown in red) that is tied to the upper wall edge, and can only move in the pink area. In the shock grid assay mice freely explored a context with a shock grid for 3 daily sessions (pre-shock, fear acquisition and fear retrieval). Shocks were delivered only on fear acquisition day. All presented shock grid data is from fear retrieval. (**B**) Assays were performed in the order described. (**C**) Bars depict behavioral metrics (n=32), for rat and fear retrieval assays, both for control and threat conditions. Wilcoxon signed-rank test; ***p<0.001.

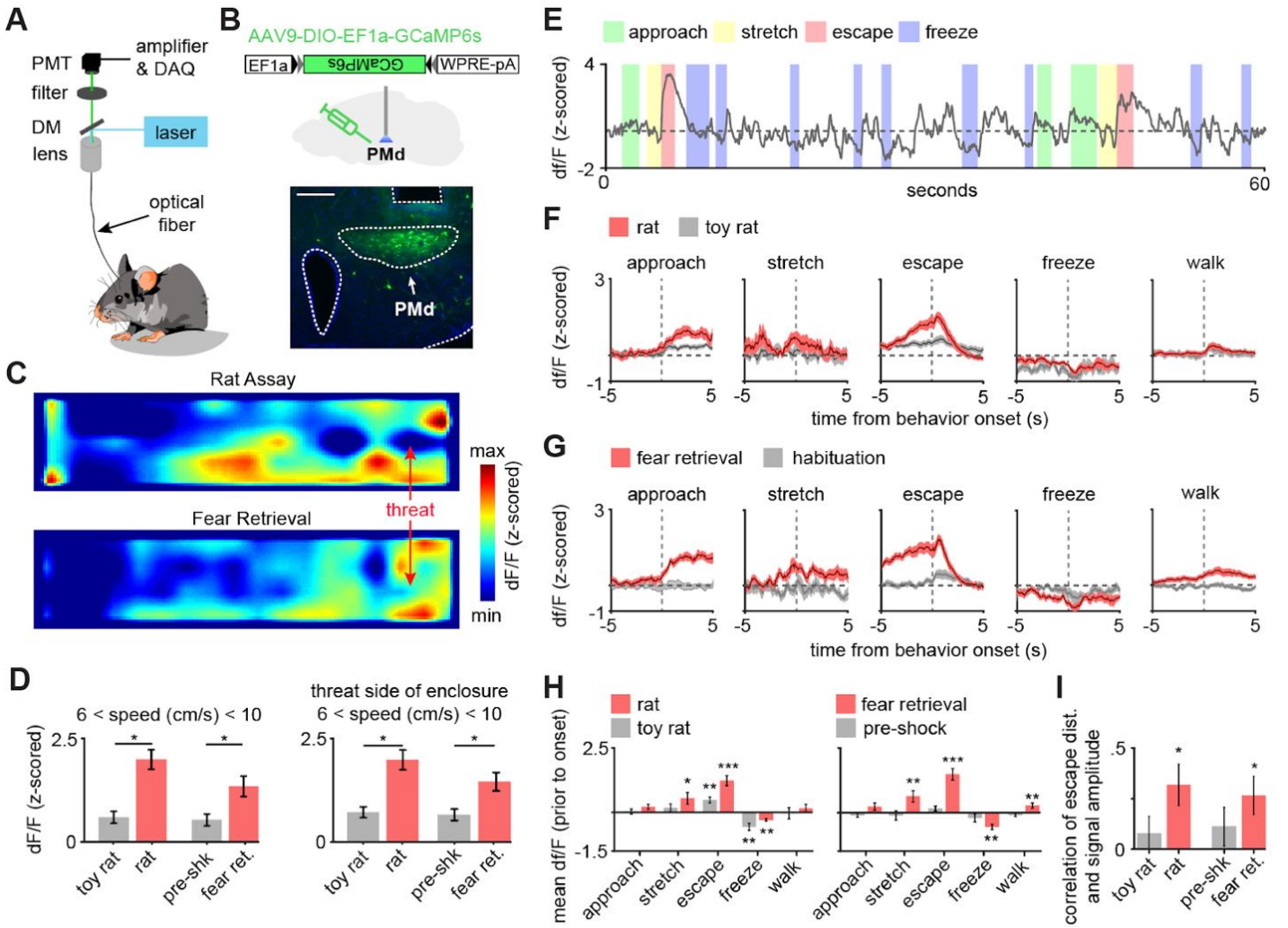

Figure 2. PMd-cck cells are activated by threats and escape. (**A**) Scheme showing setup used to obtain fiber photometry recordings. (**B**) Expression of GCaMP6s in PMd-cck cells. (Scale bar: 200 µm) (**C**) Average heatmaps showing that PMd-cck cells are more active near a rat (top) and the shock grid (bottom) (for each, n=15). (**D**) Bar graphs quantifying average z-scored df/F during exposure to the toy rat, rat, pre-shock and fear retrieval. All data are shown for the same speed range (6-10 cm/s; Wilcoxon signed-rank test) (**E**) Example GCaMP6s trace from a representative mouse showing that PMd-cck cells are active during escape. (**F**) Behavior-triggered average showing mean PMd-cck activity during approach to rat, risk-assessment stretch-attend postures, escape and freeze. (n=15 mice) (**G**) Same as (**F**), but during exposure to the fear retrieval shock grid assay. (n=15 mice) (**H**) Bars show the mean df/F from -2 to 0 seconds from behavior onset for threat (red) and control (gray) assays. (Wilcoxon signed-rank test; n (left) same as (**F**); n (right) same as (**G**)) (**I**) Bars show the Spearman correlation of the mean fiber photometry signal amplitude and distance run for all escapes. (Wilcoxon signed-rank test). (**D,H,I**), n=15 mice, data is plotted as mean +/- s.e.m. *p<0.05, **p<0.01, ***p<0.001.

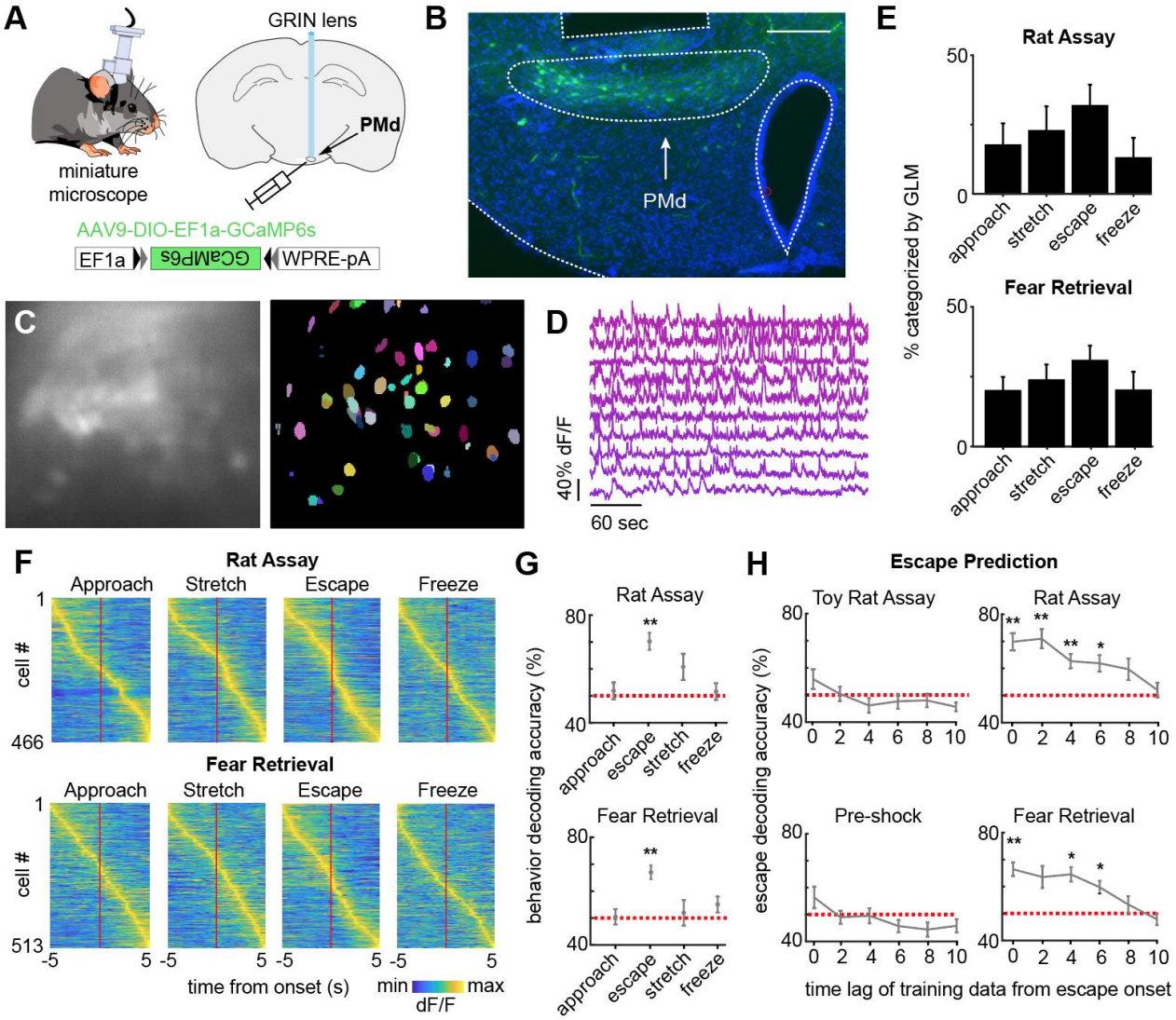

Figure 3. PMd-cck ensemble activity can predict escape in rat and shock grid fear retrieval assays. (**A**) PMd-cck mice were injected with AAV9-DIO-EF1a-GCaMP6s in the PMd and then were implanted with a miniaturized microscope. (**B**) Photo of the GCaMP6s in PMd-cck cells and location of implanted GRIN lens. (Scale bar 200 μm) (**C**) (left) Maximum projection of the PMd field of view in an example mouse. (right) Extracted cell contours for the same session. (**D**) Representative traces of a subset of calcium transients from GCaMP6s-expressing PMd-cck cells recorded in a single session. (**E**) Generalized linear models (GLMs) were used to determine GLM weights for defensive behaviors. Cells were classified as activated by each behavior based on their actual GLM weights compared to the distribution of weights generated by permuting the neural data. (n=9 mice) (**F**) Colormaps show average activation for each PMd-cck cell for each scored behavior in the rat (top) and shock grid fear retrieval (bottom) assays. Cells are sorted by time of peak activation. (**G**) Ongoing escape, but not other behaviors, can be decoded by PMd-cck cell activity in the rat (top) and shock grid fear retrieval assays (bottom) (Mice that displayed less than 5 instances of a given behavior were removed from the analysis: (top) approach n=7, stretch n=6, escape n=7, freeze n=6; (bottom) approach n=5, stretch n=4, escape n=5, freeze n=3; Wilcoxon signed-rank test). (**H**) PMd-cck cell activity can predict escape from threats, but not control stimuli, several seconds prior to escape onset. (toy rat n=8 mice, rat n=7, habituation n=5, fear retrieval n=5). (n=466 cells in rat assay, n=513 cells in shock grid fear retrieval assay; Wilcoxon signed-rank test) **p<0.01, *p<0.05.

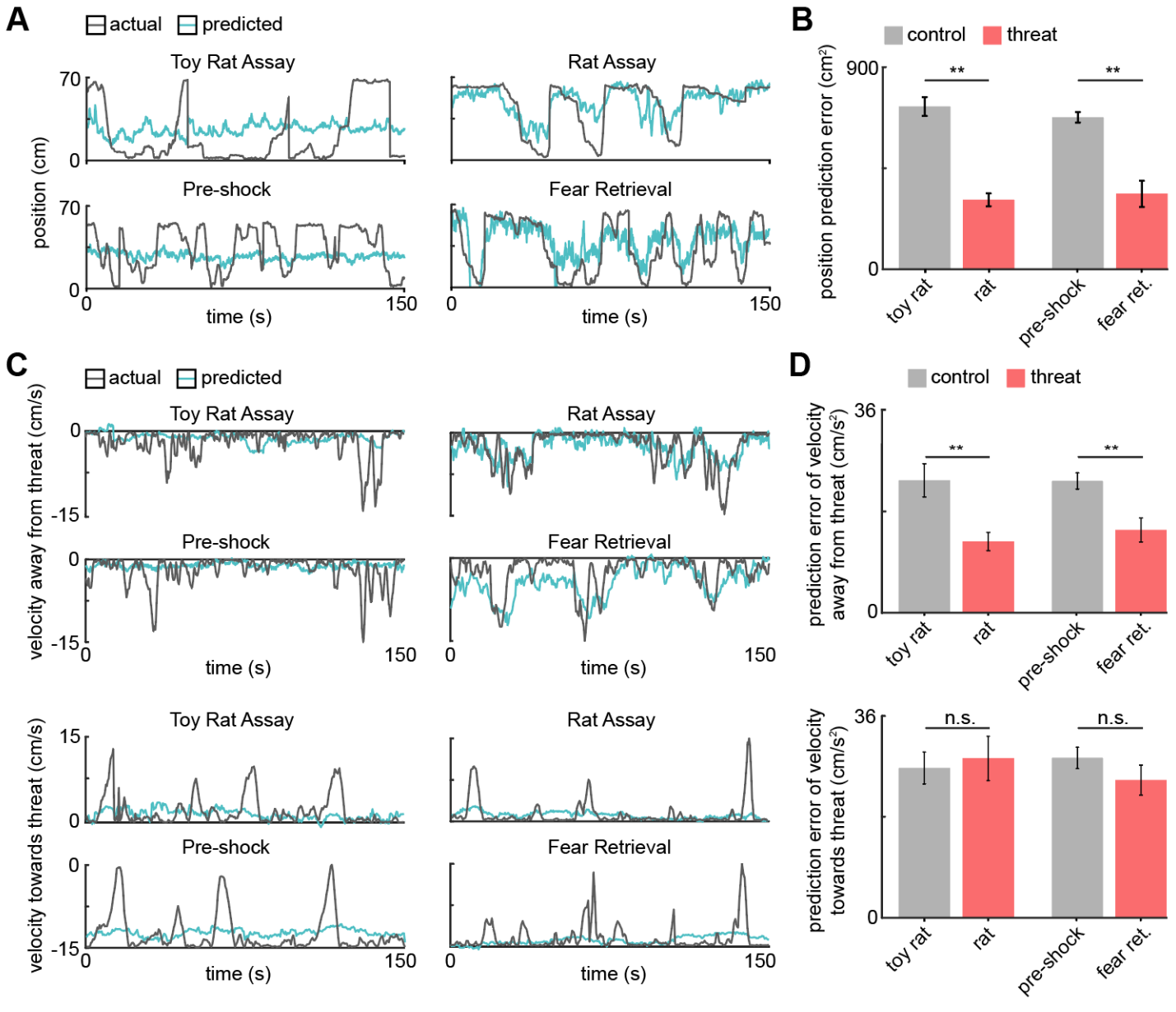

Figure 4. PMd ensemble activity represents distance from threat and escape velocity. (**A**) A general linearized model (GLM) was used to decode the position of each animal along the length of the enclosure from the neural data. The line plots depict the actual location (gray line) and GLM-predicted location (blue line) from example toy rat/rat and pre-shock/fear retrieval sessions. Note that the predicted location is more accurate for threat than control assays. (**B**) Bars show the mean squared error (MSE) of the GLM-predicted location from the actual location. The MSE is significantly lower for threat than control assays (Wilcoxon signed-rank test; n=9 mice). (**C**) Similar to (A), a GLM was used to predict the velocity away from (top) and towards (bottom) the threat in a representative mouse. (**D**) Similar to (B), bars depict the MSE of the GLM-predicted velocity away from (top) and towards (bottom) the threat. The GLM more accurately decodes threat than control velocities for samples in which the mice move away from the threat (top). The accuracy does not differ in threat and control assays for samples in which the mice move towards the threat (bottom). (Wilcoxon signed-rank test; n=9 mice) ** $p<0.01$.

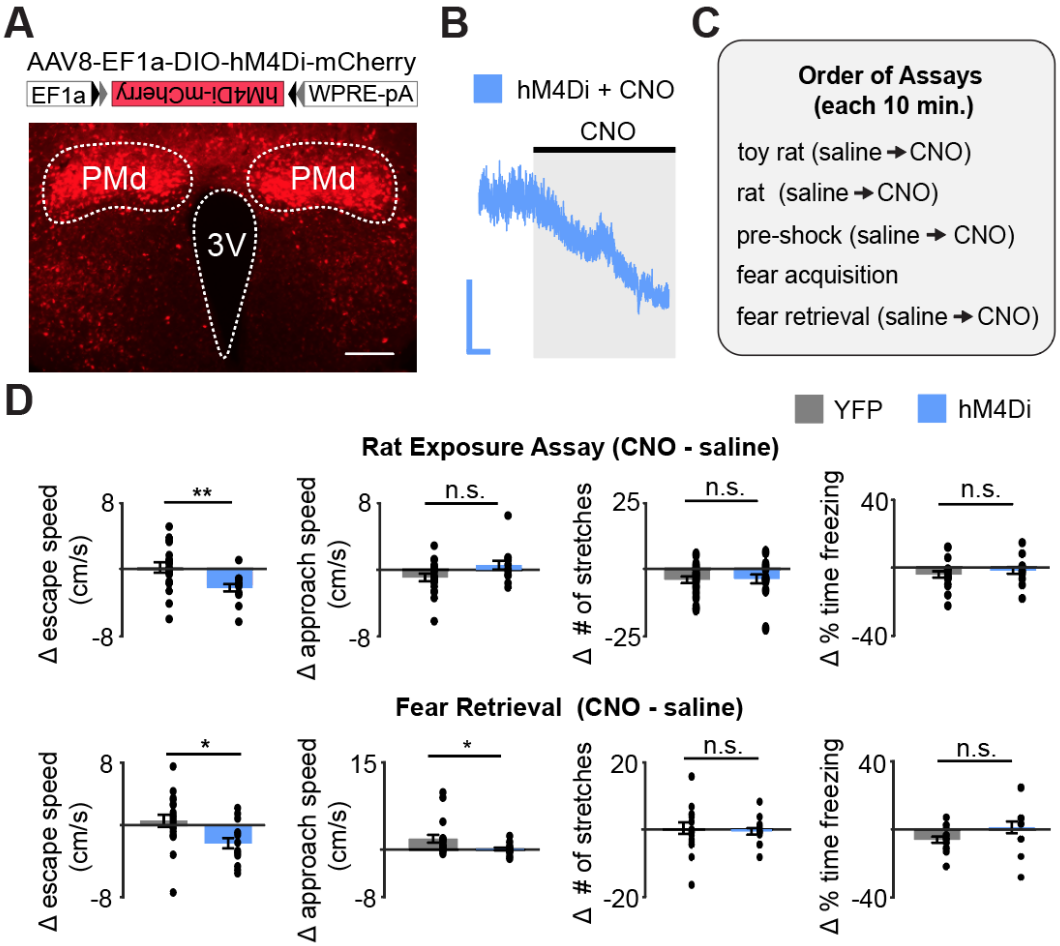

Figure 5. Chemogenetic inhibition of PMd-cck cells decreases escape speed from threats. (**A**) Cck-cre mice were injected with cre-dependent vectors encoding hM4Di-mcherry, or -mcherry in the PMd (top). Expression of hM4Di-mcherry in PMd-cck cells (bottom). (scale bar: 200 μm) (**B**) *Ex vivo* slice recordings showing that clozapine-N-oxide (CNO) hyperpolarized PMd-cck cells expressing hM4Di. (scale bar: 60s, 10 mV) (**C**) Mice were exposed to each assay twice, in the order shown, after receiving i.p. injections of either saline or CNO. (**D**) Inhibition of hM4Di-expressing PMd-cck cells decreased escape speed in the rat and fear retrieval assays. (rat exposure assay mCherry/hM4Di n=19/n=11; Wilcoxon signed-rank test) **p<0.01, *p<0.05.

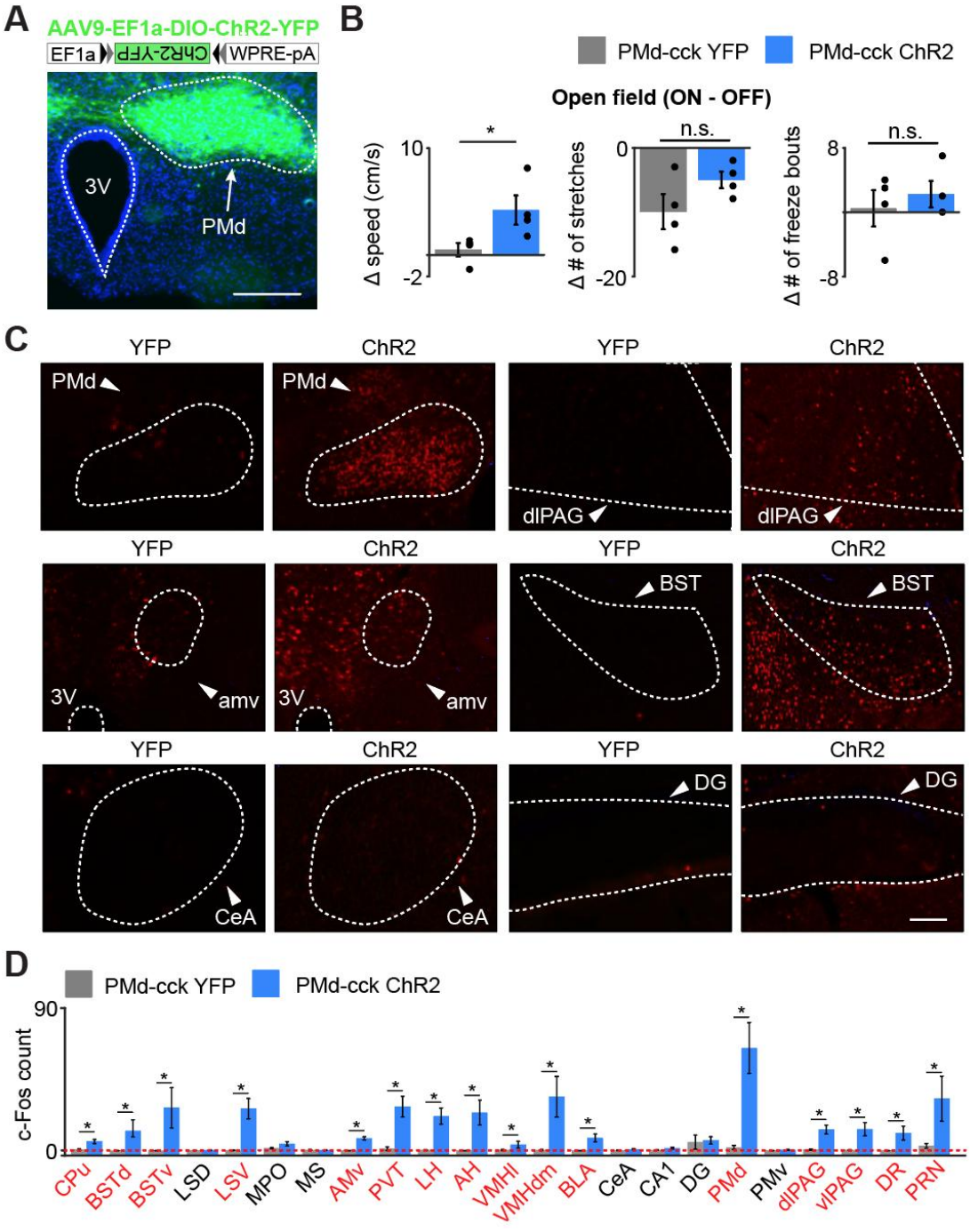

Figure 6. Optogenetic PMd-cck activation increases velocity and recruits widespread defensive networks. (**A**) Cck-cre mice were injected with AAV9-Ef1a-DIO-ChR2-YFP in the PMd (top). Expression of Chr2-YFP in PMd-cck cells (bottom; scale bar: 200 μm) (**B**) Delivery of blue light increases speed in PMd-cck ChR2 mice, but not stretch-attend postures or freeze bouts. (PMd-cck YFP n=4, PMd-cck ChR2 n=4; Wilcoxon rank-sum test). (**C**) Following optogenetic activation of PMd-cck cells mice were perfused and stained with antibodies against the immediate early gene cfos. Representative images show that blue light delivery caused increased fos expression in the PMd, bed nucleus of the stria terminalis (BST) and anteromedial ventral thalamus (amv). Other regions, such as the central amygdala (Cea) and the dentate gyrus (DG) did not show increased fos expression following PMd-cck optogenetic stimulation. (scale bar: 100 μm) (**D**) Average number of fos-expressing cells in various brain regions following light delivery to

ChR2 (blue) or YFP (gray)-expressing cells. Regions for which the c-Fos count is significantly greater for ChR2 than YFP mice are labelled in red. (Wilcoxon rank-sum test, PMd-cck YFP n=5, PMd-cck ChR2 n=4) *p<0.05. Abbreviations: CPu (caudate-putamen), BSTd/v (dorsal and ventral bed nucleus of the stria terminalis), LS D/V (dorsal and ventral lateral septum), MPO (medial preoptic area), amv (anteromedial ventral thalamus), PVT (paraventricular nucleus of the hypothalamus), LH (lateral hypothalamus), AH (anterior hypothalamus), VMHvl/dm (ventrolateral and dorsomedial portions of the ventromedial hypothalamus), BLA (basolateral amygdala), CeA (central amygdala), CA1 (hippocampal cornus ammonis 1), DG (dentate gyrus), PMd (dorsal premammillary nucleus), PMv (ventral premammillary nucleus), dlPAG (dorsolateral periaqueductal gray), vlPAG (ventrolateral periaqueductal gray), DR (dorsal Raphe), PRN (pontine reticular nucleus)

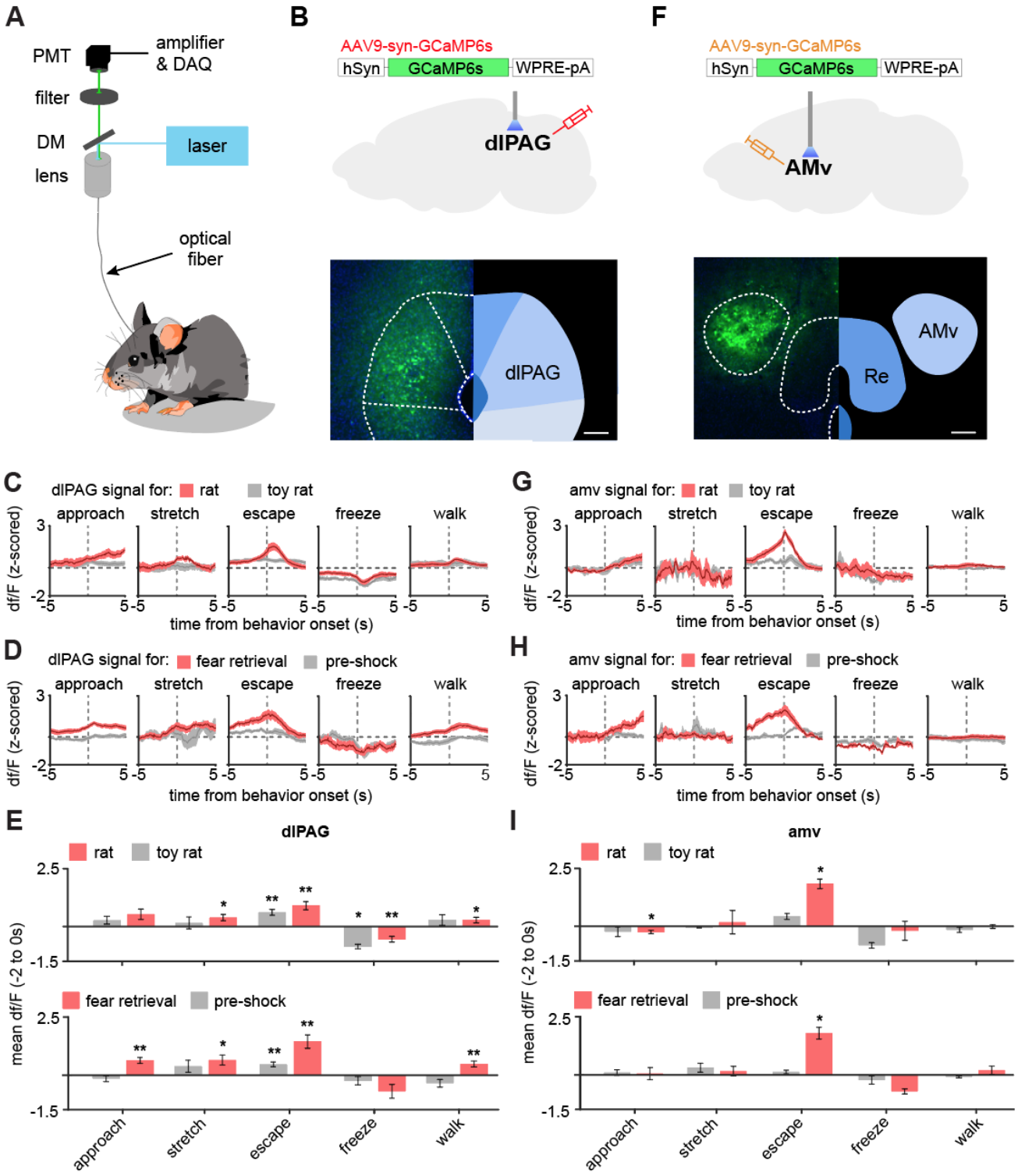

Figure 7. The dlPAG and AMV are activated by threats and escape. (**A**) Scheme showing setup used to obtain fiber photometry recordings. (**B**) Expression of GCaMP6s in the dlPAG. (Scale bar: 150µm) (**C**) Behavior-triggered average showing mean dlPAG activity during approach to rat, risk-assessment stretch-attend postures, escape, freeze and walking perpendicularly to the rat at the safe side of the enclosure. (n=9 mice) (**D**) Same as (**C**), but during exposure to the fear retrieval shock grid assay. (n=9 mice) (**E**) Bars show the mean df/F from -2 to 0 seconds from behavior onset for threat (red) and control (gray) assays. (n=9 mice). (**F-I**) Same as (**B-E**), but for the amv. (**F**) Scale bar: 150µm (**G-I**) n=6 mice. (**E,F**) Wilcoxon signed-rank test; **p<0.01, *p<0.05.

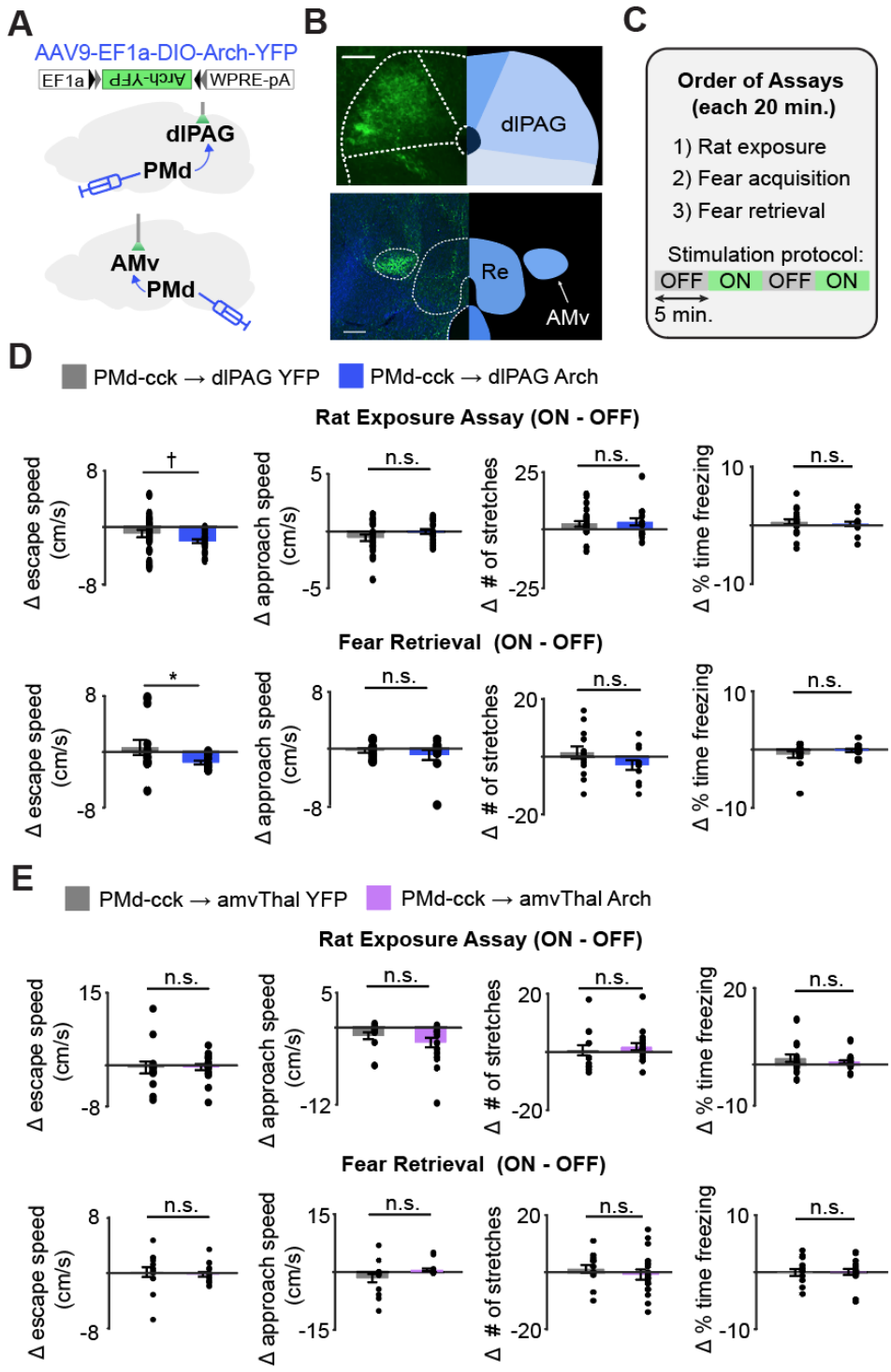

Figure 8. Optogenetic inhibition of the PMd-cck projection to the dlPAG, not the amv, decreases escape velocity during exposure to innate and conditioned threats. (**A**) Viral vectors were used to express Arch in PMd-cck cells. Fiber optic cannula were bilaterally implanted over PMdc-cck arch-expressing axon terminals in the amv or dlPAG. (**B**) Image showing PMd-cck axon terminals expressing arch-YFP in the dlPAG and amv. (Scale bars: 150µm) (**C**) Summary diagram showing order of assays and green light delivery protocol. (**D**) Inhibition of the PMd-cck projection to the dlPAG decreased escape speed, but not other defensive behaviors. (Wilcoxon rank-sum test; (top) rat exposure assay: YFP/Arch n=24/n=12; (bottom) fear retrieval: YFP/Arch n=14/n=11) (**E**) Inhibition of the PMd-cck projection to the amv did not alter any of the behavioral measures monitored. (Wilcoxon rank-sum test; (top) rat exposure assay: YFP/Arch n=12/n=18; (bottom) fear retrieval: YFP/Arch n=12/n=17), *p<0.05; † p=0.058.

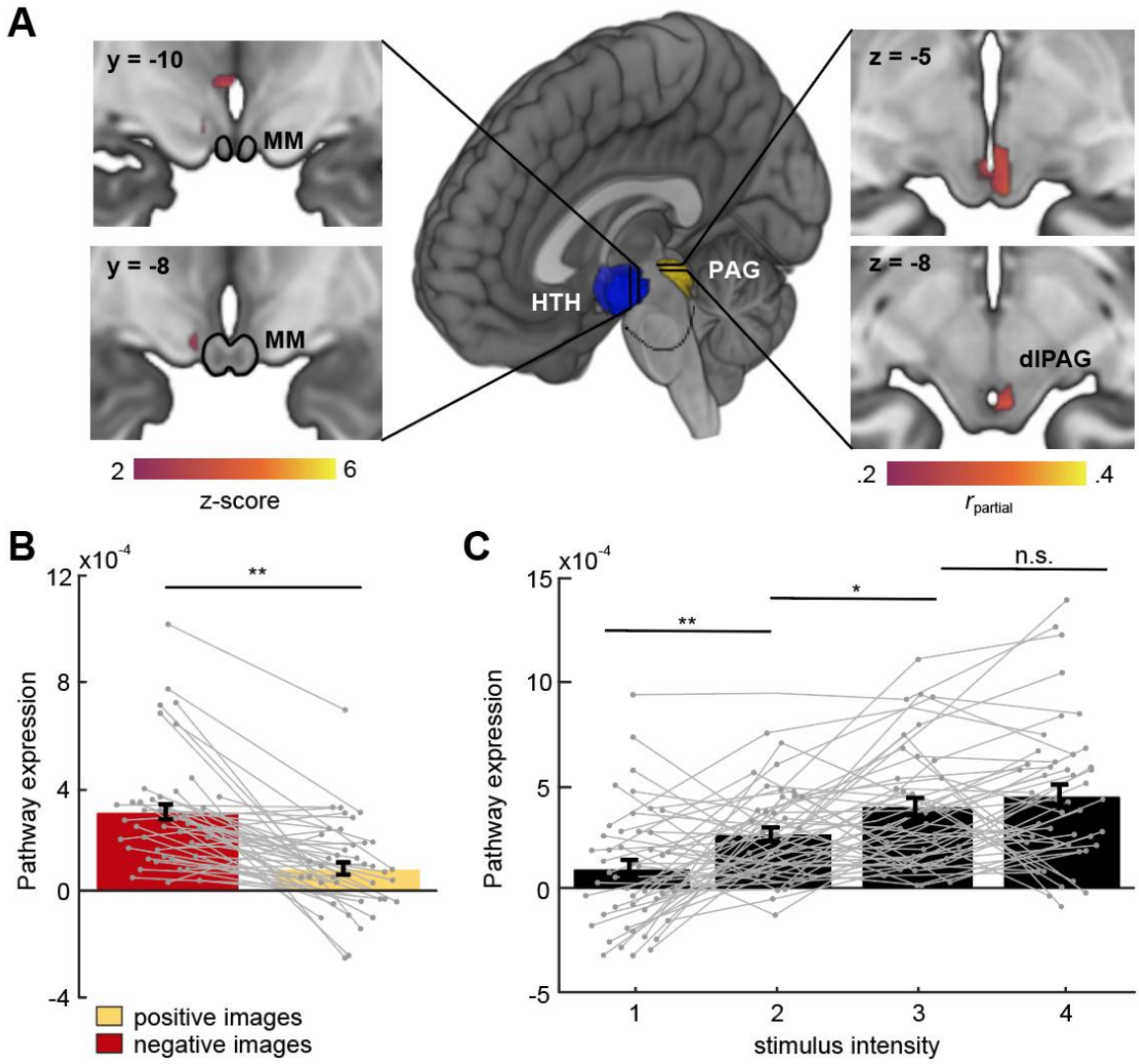

Figure 9. Hypothalamus (HTH)-PAG pathway is sensitive to aversive visual stimuli in humans. (**A**) Multivariate brain pathway estimated using activation in the hypothalamus (HTH, rendered in blue) to predict patterns of activation in the periaqueductal gray (PAG, rendered in yellow). Inserts depict statistical maps indicating which regions of the HTH covaried most strongly with the PAG (left) and portions of dorsal PAG (dlPAG) that were explained by the HTH but not a pathway from the central amygdala. The mammillary bodies (MM) are depicted with a black outline. Note that all hypothalamus voxels are included in the model, only suprathreshold voxels are shown here. (**B**) Average bar plot showing that the HTH-PAG pathway was more active during exposure to threat (aversive visual images) compared to control stimuli (non-aversive, positive images). Each circle corresponds to an individual subject. (**C**) Pathway expression monotonically increased as a function of stimulus intensity. Inference on brain maps is based on bootstrap resampling of regression coefficients from pathway estimation (left) and partial correlation coefficients (right). All maps are thresholded at $q_{FDR} < .05$. (Wilcoxon signed-rank test, n = 48 participants) **p<0.001, *p<0.01.

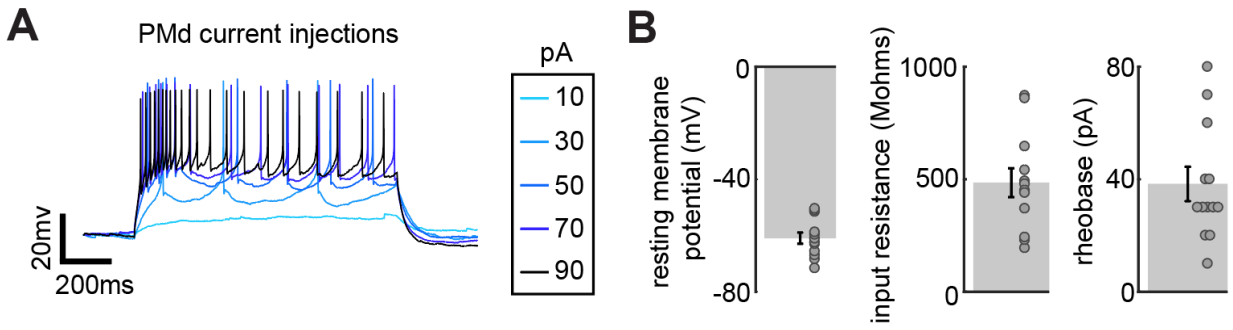

Figure 2, figure supplement 1. Characterization of *PMd-cck* cell biophysical properties in acute slices. Mice from a cck-cre driver line were injected with cre-dependent viral vectors encoding YFP in the PMd. Acute slices were prepared from these mice and YFP-expressing cells in the PMd were used to measure biophysical properties of PMd-cck cells. (**A**) Injection of current triggers action potentials in PMd cells. (**B**) Average resting membrane potential, input resistance and rheobase in PMd cells (n=12 cells).

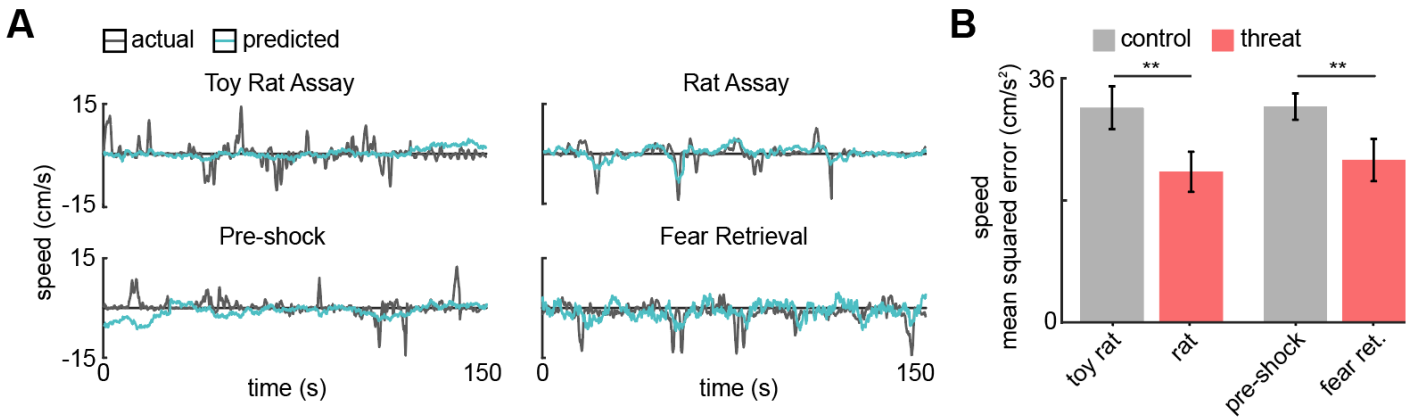

Figure 4, figure supplement 1. PMd ensemble activity represents speed in threat assays. (**A**) A GLM was used to predict the speed of a representative mouse. (**B**) Bars depict the mean squared error (MSE) of the GLM-predicted speed. The GLM more accurately decodes threat than control speeds. (Wilcoxon signed-rank test; n=9 mice) ** p<0.01.

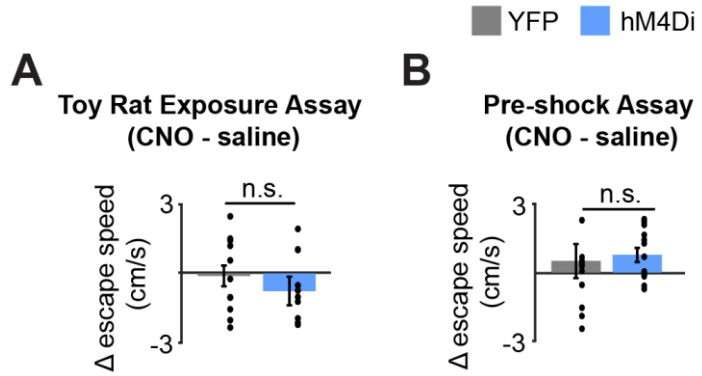

Figure 5, figure supplement 1. Inhibition of PMd-cck cells does not affect escape speed in control assays. (**A**) Bars depict the change in escape speed (CNO-saline) during toy rat exposure assay (Wilcoxon rank-sum test; mCherry/hM4Di n=7/n=8). (**B**) Bars depict the change in escape speed (CNO-saline) during pre-shock assay (Wilcoxon rank-sum test; mCherry/hM4Di n=7/n=12).

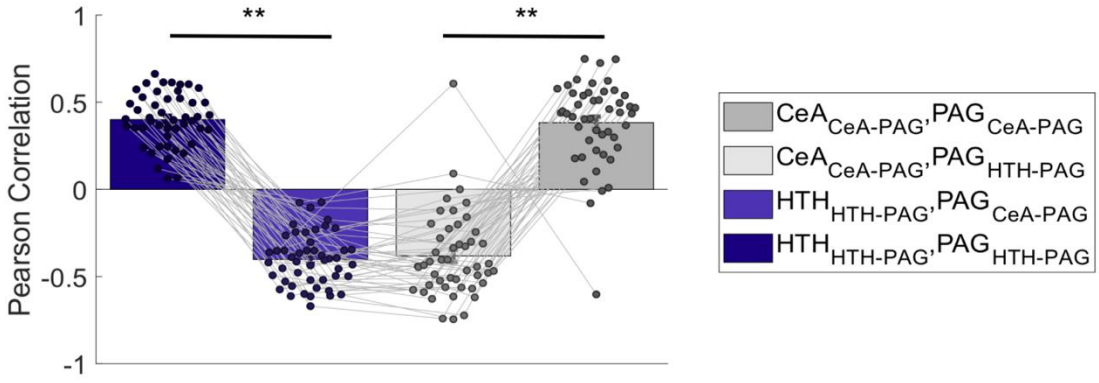

Figure 9, figure supplement 1. Multi-voxel response patterns in the PAG related to hypothalamus (HTH) and central amygdala (CeA) are functionally distinct. The HTH pattern optimized for PAG connectivity ([$HTH_{HTH\text{-}PAG}$]) correlates positively with its respective PAG pattern ([$PAG_{HTH\text{-}PAG}$]) in 100% of test subjects (dark blue), but negatively with a PAG pattern optimized to covary with CeA ([$PAG_{CeA\text{-}PAG}$]; light blue). Conversely, The CeA pattern optimized for PAG connectivity ([$CeA_{CeA\text{-}PAG}$]) correlates positively with its respective PAG pattern in in >90% of test subjects ([$PAG_{CeA\text{-}PAG}$]; dark gray), but negatively with a PAG pattern optimized to covary with HTH ([$PAG_{HTH\text{-}PAG}$]; light gray). This double dissociation shows that the HTH-PAG and CeA-PAG pathways are functionally distinct in human participants, and even oppose one another. Each circle corresponds to an individual subject. Wilcoxon signed-rank test; $^{**}P < .001$. (n=48 participants)

Methods

All procedures conformed to guidelines established by the National Institutes of Health and have been approved by the University of California, Los Angeles Institutional Animal Care and Use Committee or by the University of Sao Paulo Animal Bioethics committee.

Mice. Cck-IRES-Cre mice (Jackson Laboratory stock No. 012706) and wild type C57BL/6J mice (Jackson Laboratory stock No. 000664) were used for all experiments. Male and female mice between 2 and 6 months of age were used in all experiments. Mice were maintained on a 12-hour reverse light-dark cycle with food and water ad libitum. Sample sizes were chosen based on previous behavioral optogenetics studies on defensive behaviors, which typically use 6-15 mice per group. All mice were handled for a minimum of 5 days prior to any behavioral task.

Rats. Male Long-Evans rats (250-400 grams) were obtained from Charles River Laboratories and were individually housed on a standard 12-hour light-dark cycle and given food and water *ad libitum*. Rats were only used as a predatory stimulus. Rats were handled for several weeks prior to being used and were screened for low aggression to avoid attacks on mice. No attacks on mice were observed in this experiment.

Viral Vectors. All vectors were purchased from Addgene.

Optogenetics: AAV9.EF1a.DIO.hChR2(H134R)-eYFP.WPRE.hGH, AAV9-EF1a-DIO-eYFP and AAV9-Ef1a-DIO-Arch-GFP.
Chemogenetics: pAAV8-hSyn-DIO-hM4D(Gi)-mCherry and AAV8.Syn.DIO. mCherry
Fiber Photometry AAV9.Syn.GCaMP6s.WPRE.SV40 and AAV9.Syn.FLEX.GCaMP6s.WPRE.SV40

Surgeries. Surgeries were performed as described previously (Adhikari et al., 2015). Eight-week-old mice were anaesthetized with 1.5-3.0% isoflurane and placed in a stereotaxic apparatus (Kopf Instruments). A scalpel was used to open an incision along the midline to expose the skull. After performing a craniotomy, 40 nl of one of the viral vectors listed above at a titer of 2*1012 particles/ml was injected per site (PMd, amv dlPAG) using a 10 µl nanofil syringe (World Precision Instruments) at 0.08 µl/min. The syringe was coupled to a 33-gauge beveled needle, and the bevel was placed to face the anterior side of the animal. The syringe was slowly retracted 20 minutes after the start of the infusion. Mice received unilateral viral infusion and fiber optic cannula implantation. Infusion locations measured as anterior-posterior, medial-lateral and dorso-ventral coordinates from bregma were: dorsolateral periaqueductal gray (dlPAG) (-4.75, -0.45, -1.9), dorsal premammillary nucleus (PMd) (-2.46, -0.5, -5.35) and anteromedial ventral thalamus (amv) (-0.85, -0.5, -3.9). For optogenetic experiments, fiber optic cannula (0.22 NA, 200 µm diameter; Newdoon) were implanted bilaterally 0.15 mm above the viral infusion sites. Only mice with viral expression restricted to the intended targets were used for behavioral assays.

For photometry experiments mice were injected with 0.16 uL at a titer of $3*10^{12}$ of AAV9.Syn.Flex.GCaMP6s.WPRE.SV40 in the PMd of cck-cre mice. The same volume and titer of AAV9.Syn.GCaMP6s.WPRE.SV40 was injected into the dlPAG or amv. Mice were implanted unilaterally with fiberoptic cannulae in the PMd, amv dlPAG. A 400 µm diameter, 0.48 NA optical fiber

(Neurophotometrics) was used for photometry experiments. Adhesive cement (C&B metabond; Parkell, Edgewood, NY, USA) and dental cement (Stoelting, Wood Dale, IL, USA) were used to securely attach the fiber optic cannula to the skull. For miniaturized microscope experiments 40 nL of AAV9-DIO-GCaMP6s was injected in the PMd of cck-cre mice and a 7mm GRIN lens was implanted 200 uM above the infusion site. Three weeks following surgery animals were base-plated.

Rat Exposure Assay. Mice were accustomed to handling prior to any behavioral assay. On day 1, mice were habituated to a white rectangular box (70 cm length, 26 cm width, 44 cm height) for 20 minutes. Twenty-four hours later, mice were exposed to the same environment but in the presence of a toy rat for 20 minutes. Mice were then exposed to an adult rat or a toy rat in this environment on the two following days. The rat was secured by a harness tied to one of the walls and could freely ambulate only within a short radius of approximately 20 cm. The mouse was placed near the wall opposite to the rat and freely explored the context for 20 minutes. No separating barrier was placed between the mouse and the rat, allowing for close naturalistic encounters that can induce a variety of robust defensive behaviors.

Contextual Fear Conditioning Test. To better evaluate a broader species-specific defense repertoire in face of a conditioned stimulus, we used a modified version of the standard contextual fear conditioning method (Schuette et al., 2020). Pre-shock, fear conditioning and retrieval sessions were performed in a context (70 cm x 17 cm x 40 cm) with an evenly distributed light intensity of 40 lux and a Coulbourn shock grid (19.5 cm x 17 cm) set at the extreme end of the enclosure. Forty-eight hours after rat exposure, mice were habituated to this context and could freely explore the whole environment for 20 minutes. On the following day, the grid was activated, such that a single 0.7 mA foot shock was delivered for 2 seconds only on the first time the mouse fully entered the grid zone. Twenty-four hours later, retrieval sessions were performed in the same enclosure but without shock. Mice could freely explore the context for 20 minutes during pre-shock habituation, fear conditioning and retrieval sessions.

Behavioral quantification. To extract the pose of freely-behaving mice in the described assays, we implemented DeepLabCut (Nath et al., 2019), an open-source convolutional neural network-based toolbox, to identify mouse nose, ear and tailbase xy-coordinates in each recorded video frame. These coordinates were then used to calculate velocity and position at each timepoint, as well as classify behaviors such as escape runs and freezes in an automated manner using custom Matlab scripts. Specifically:

'Escapes' were defined as epochs for which (1) the mouse speed away from the rat or toy rat exceeded 2 cm/s. As there was little room for acceleration between the rat and opposite wall, the speed threshold was set to this relatively low value.

'Stretch-attend postures' were defined as epochs for which (1) the distance between mouse nose and tailbase exceeded a distance of approximately 1.2 mouse body lengths and (2) mouse tailbase speed fell below 1 cm/s.

'Freezes' were defined as periods for which mouse nose and tailbase speed fell below 0.25 cm/s for at least 0.33s (Schuette et al., 2020).

All behaviors were manually checked by the experimenters for error.

Fiber photometry. Photometry was performed as described in detail previously (Kim et al., 2016). Briefly, we used a 405-nm LED and a 470-nm LED (Thorlabs, M405F1 and M470F1) for the Ca^{2+}-dependent and Ca^{2+}independent isosbestic control measurements. The two LEDs were bandpass filtered (Thorlabs, FB410-10 and FB470-10) and then combined with a 425-nm longpass dichroic mirror (Thorlabs, DMLP425R) and coupled into the microscope using a 495-nm longpass dichroic mirror (Semrock, FF495-Di02-25 ×36). Mice were connected with a branched patch cord (400 µm, Doric Lenses, Quebec, Canada) using a zirconia sleeve to the optical system. The signal was captured at 20 Hz (alternating 405-nm LED and 470-nm LED). To correct for signal artifacts of a non biological origin (i.e. photobleaching and movement artifacts), custom Matlab scripts leveraged the reference signal (405-nm), unaffected by calcium saturation, to isolate and remove these effects from the calcium signal (470-nm).

Fiber Photometry behavior-triggered averaging. To plot the behavior-triggered averages, only mice that displayed a minimum of three behavioral instances were included in the corresponding behavioral figure.

Miniscope video capture. All videos were recorded at 30 frames/sec using a Logitech HD C310 webcam and custom-built head-mounted UCLA miniscope (Cai et al., 2016). Open-source UCLA Miniscope software and hardware (http://miniscope.org/) were used to capture and synchronize neural and behavioral video (Cai et al., 2016).

Miniscope postprocessing. The open-source UCLA miniscope analysis package (https://github.com/daharoni/Miniscope_Analysis) (Aharoni and Hoogland, 2019) was used to motion correct miniscope videos. They were then temporally downsampled by a factor of four and spatially downsampled by a factor of two. The cell activity and footprints were extracted using the open-source package Constrained Nonnegative Matrix Factorization for microEndoscopic data (CNMF-E; https://github.com/zhoupc/CNMF_E) (Schuette et al., 2020; Zhou et al., 2018). Only cells whose variance was greater than or equal to 25% of the maximum variance among non-outliers were used in the analysis.

Behavior decoding using PMd neural data. Discrete classification of escape behavior was performed using multinomial logistic regression. Timepoints following escape by 2 seconds were labelled 'escape,' and a matched number of non-escape timepoints were randomly selected for training and validation. Each time point was treated as an individual data point. Training and validation were performed using 5-fold cross-validation, with a minimum of 10 seconds between training and validation sets. As equal numbers of escape and non-escape samples were used to build the training and validation sets, chance accuracy was 50%. Sessions with less than 5 escapes were excluded from the analysis. The same analysis was performed for approach, stretch-attend postures, and freeze. To predict escape at negative time lags from behavior onset, the same analysis procedure was implemented, using 2-second epochs preceding escape by 2, 4, 6, 8 and 10 seconds.

Behavior cell classification. We used a generalized linear model (GLM) to identify cells that showed increased calcium activity during approach, stretch-attend, escape and freeze behaviors. We fit this model to each cell's activity, with behavior indices as the predictor variable and behavior coefficients as

the measure of fit. Behavior onset times were then randomized 100 times and a bootstrap distribution built from the resulting GLM coefficients. A cell was considered a behavior-categorized cell if its coefficient exceeded 95% of the bootstrap coefficient values.

Position and speed decoding. To predict position and speed from neural data, these data had their dimensionality reduced by principal component analysis, such that the top principal components, representing at least 80% of the total variance, were used in the following decoding analysis. This output and the related position/speed data were then separated into alternating 60s training and testing blocks, with 10s of separation between blocks. Even blocks were used to train a generalized linear regression model (GLM; Matlab function 'glmfit') and withheld odd blocks were used to test the resulting model. Accuracies of this withheld testing block were reported as mean squared error.

Chemogenetics. Mice used for chemogenetic experiments were exposed to each threat and control stimuli twice, once following treatment with saline and once following treatment with CNO (5 mg/kg, injected intraperitoneally) 40 minutes prior to the experiment. Only one control or threat-exposure assay was performed per day with each mouse.

Behavior video capture. All behavior videos were captured at 30 frames/sec in standard definition (640x480) using a Logitech HD C310 webcam. To capture fiber-photometry synchronized videos, both the calcium signal and behavior were recorded by the same computer using custom Matlab scripts that also collected timestamp values for each calcium sample/behavioral frame. These timestamps were used to precisely align neural activity and behavior.

Light Delivery for optogenetics. For PMd-cck ChR2 mice, blue light was generated by a 473 nm laser (Dragon Lasers, Changchun Jilin, China) at 4.5 mW unless otherwise indicated. Green light was generated by a 532 nm laser (Dragon Lasers), and bilaterally delivered to mice at 10 mW. A Master-8 pulse generator (A.M.P.I., Jerusalem, Israel) was used to drive the blue laser at 20 Hz. This stimulation pattern was used for all ChR2 experiments. The laser output was delivered to the animal via an optical fiber (200 µm core, 0.22 numerical aperture, Doric Lenses, Canada) coupled to the fiberoptic implanted on the animals through a zirconia sleeve.

Immunostaining for cfos. Fixed brains were kept in 30% sucrose at 4°C overnight, and then sectioned on a cryostat (40 µm) slices. Sections were washed in PBS and incubated in a blocking solution (3% normal donkey serum and 0.3% triton-x in PBS) for 1 hour at room temperature. Sections were then incubated at 4oC for 12 hours with polyclonal anti-fos antibody made in rabbit (1/500 dilution) (c-Fos (9F6) Rabbit mAb CAT#2250, Cell Signalling Technology) in blocking solution. Following primary antibody incubation sections were washed in PBS 3 times for 10 minutes, and then incubated with anti-rabbit IgG (H+L) antibody (1/500 dilution) conjugated to Alexa Fluor 594 (red) (CAT# 8889S, cellsignal.com) for 1 hour at room temperature. Sections were washed in PBS 3 times for 10 minutes, incubated with DAPI (1/50000 dilution in PBS), washed again in PBS and mounted in glass slides using PVA-DABCO (Sigma).

Perfusion and histological verification. Mice were anesthetized with Fatal-Plus and transcardially perfused with phosphate buffered saline followed by a solution of 4% paraformaldehyde. Extracted

brains were stored for 12 hs at 4°C in 4% paraformaldehyde. Brains were then placed in sucrose for a minimum of 24 hs. Brains were sectioned in the coronal plane in a cryostat, washed in phosphate buffered saline and mounted on glass slides using PVA-DABCO. Images were acquired using a Keyence BZ-X fluorescence microscope with a 10 or 20X air objective.

Acute brain slice preparation and electrophysiological recordings. Cck-cre driver line mice were injected with AAV9-FLEX-ChR2-YFP in the PMd. Acute slices were prepared from these mie. For electrophysiological measurements, slices were transferred as needed to the recording chamber, where they were perfused with oxygenated aCSF at 32°C. The slices were held in place using a nylon net stretched within a U-shaped platinum wire. Visually-guided whole cell patch clamp recordings were made using infrared differential interference contrast optics. We also verified the identity of PMD neurons by only recording from YFP-positive neurons. All recordings were obtained using a MultiClamp 700B amplifier system (Molecular Devices, Union City, CA). Experiments were controlled by PClamp 10 software running on a PC, and the data were acquired using the Digidata 1440A acquisition system. All recording electrodes (3-8 MΩ) were pulled from thin-walled capillary glass (A-M Systems, Carlsborg, WA) using a Sutter Instruments P97 puller. The patch pipettes were filled with internal solution containing (in mM) 100 K- gluconate, 20 KCl, 4 ATP-Mg, 10 phospho-creatine, 0.3 GTP-Na, and 10 HEPES (in mM) with a pH of 7.3 and osmolarity of 300 mOsm. Only cells with a stable, uncorrected resting membrane potential (RMP) between -50 to -80 mV, overshooting action potentials, and an input resistance (RN) > 100 MW were used. To minimize the influence of voltage-dependent changes on membrane conductances, all cells were studied at a membrane potential near -60 mV (using constant current injection under current clamp mode). To study intrinsic firing properties of PMD neurons, WCRs were conducted under current clamp using the following protocol: (1) Voltage–current (V-I) relations were obtained using 400 ms current steps (range -50 pA to rheobase) and by plotting the plateau voltage deflection against current amplitude. Neuronal input resistance (RN) was determined from the slope of the linear fit of that portion of the V-I plot where the voltage sweeps did not exhibit sags or active conductance. (2) Intrinsic excitability measurements were obtained using 1s current steps (range 0 to 500 pA) and by plotting the number of action potentials fired against current amplitude. (3) Resting membrane potential (RMP) was calculated as the difference between mean membrane potential during the first minute immediately after obtaining whole cell configuration and after withdrawing the electrode from the neuron.

For validating hM4Di in PMd-cck cells, acute brain slices preparation and electrophysiological recordings were performed using standard methods as previously described (Nagai et al., 2019). Briefly, Cck-Cre+ mice that had received AAV microinjections into PMd were deeply anesthetized with isoflurane and decapitated with sharp shears. The brains were placed and sliced in ice-cold modified artificial CSF (aCSF) containing the following (in mM): 194 sucrose, 30 NaCl, 4.5 KCl, 1 $MgCl_2$, 26 $NaHCO_3$, 1.2 $NaH2PO_4$, and 10 D-glucose, saturated with 95% O_2 and 5% CO_2. A vibratome (DSK-Zero1) was used to cut 300 µm brain sections. The slices were allowed to equilibrate for 30 minutes at 32-34°C in normal aCSF containing (in mM); 124 NaCl, 4.5 KCl, 2 $CaCl_2$, 1 $MgCl_2$, 26 $NaHCO_3$, 1.2 NaH_2PO_4, and 10 D-glucose continuously bubbled with 95% O_2 and 5% CO_2. Slices were then stored at 21–23°C in the same buffer until use. All slices were used within 2-6 hours of slicing.

Slices were placed in the recording chamber and continuously perfused with 95% O_2 and 5% CO_2 bubbled normal aCSF. pCLAMP10.4 software and a Multi-Clamp 700B amplifier was used for electrophysiology (Molecular Devices). Whole-cell patch-clamp recordings were made from neurons in the PMd or dorsolateral PAG (dlPAG) using patch pipettes with a typical resistance of 4–5 MΩ. Neurons were selected based on reporter fluorescence,(mCherry for hM4Di-mCherry). The intracellular solution for recordings comprised the following (in mM) : 135 potassium gluconate, 5 KCl, 0.5 $CaCl_2$, 5 HEPES, 5 EGTA, 2 Mg-ATP and 0.3 Na-GTP, pH 7.3 adjusted with KOH. The initial access resistance values were < 20 MΩ for all cells; if this changed by > 20% the cell was discarded. Light flashes (0.2 mW/mm2) from a blue LED light source (Sutter Instruments) were delivered via the microscope optics and a 40x water immersion objective lens and controlled remotely using TTL pulses from Clampex. Cell responses were recorded in whole-cell mode and recorded using an Axopatch 700B amplifier connected via a digitizer to a computer with pCLAMP10 software. To stimulate ChR2 expressed in PMd neurons or axons, 5 ms pulses were delivered at inter-pulse intervals of 200 ms, 50 ms or 25 ms for 5, 20 or 40 Hz optical stimulations, respectively.

Functional Magnetic Resonance Imaging (fMRI) methods

Participants. This study included 48 adult participants (mean ± SD age: 25.1 ± 7.1; 27 male, 21 female; 7 left-handed; 40 white and 8 non-white (1 Hispanic, 5 Asian, 1 Black and 1 American Indian)). All participants were healthy, with normal or corrected to normal vision and normal hearing, and with no history of psychiatric, physiological or pain disorders and neurological conditions, no current pain symptoms and no MRI contraindications. Eligibility was assessed with a general health questionnaire, a pain safety screening form and an MRI safety screening form. Participants were recruited from the Boulder/Denver Metro Area. The institutional review board of the University of Colorado Boulder approved the study, and all participants provided written informed consent.

Experimental Paradigm. Participants received five different types of aversive stimulation (mechanical pain, thermal pain, aversive auditory, aversive visual, and pleasant visual), each at four stimulus intensities. 24 stimuli of each type (6 per intensity) were presented over six fMRI runs in random order. Following stimulation on each trial, participants made behavioral ratings of their subjective experience. Participants were instructed to answer the question 'How much do you want to avoid this experience in the future?'. Ratings were made with a non-linear visual analog rating scale, with anchors 'Not at all' and 'Most' displayed at the ends of the scale.

Stimuli. Visual stimulation was administered on the MRI screen and included normed images from the International Affective Picture System (IAPS) database (Lang et al., 2008). To induce four 'stimulus intensity levels' we selected four groups of 7 images based on their normalized aversiveness ratings (averaged across male and female raters) available in the IAPS database and confirmed by N = 10 lab members (5 male, 5 female) in response to 'How aversive is this image? 1-100'. Selected images included photographs of animals (n=7), bodily illness and injury (n=12), industrial and human waste (n=9). Four stimulus levels were delivered to participants for 10 sec each.

MRI data acquisition and preprocessing. Whole-brain fMRI data were acquired on a 3T Siemens MAGNETOM Prisma Fit MRI scanner at the Intermountain Neuroimaging Consortium facility at the University of Colorado, Boulder. Structural images were acquired using high-resolution T1 spoiled

gradient recall images (SPGR) for anatomical localization and warping to standard MNI space. Functional images were acquired with a multiband EPI sequence (TR = 460 ms, TE = 27.2 ms, field of view = 220 mm, multiband acceleration factor = 8, flip angle = 44°, 64 × 64 image matrix, 2.7 mm isotropic voxels, 56 interleaved slices, phase encoding posterior >> anterior). Six runs of 7.17 mins duration (934 total measurements) were acquired. Stimulus presentation and behavioral data acquisition were controlled using Psychtoolbox.

FMRI data were preprocessed using an automated pipeline implemented by the Mind Research Network, Albuquerque, NM. Briefly, the preprocessing steps included: distortion correction using FSL's top-up tool (https://fsl.fmrib.ox.ac.uk/fsl/), motion correction (affine alignment of first EPI volume (reference image) to T1, followed by affine alignment of all EPI volumes to the reference image and estimation of the motion parameter file (sepi_vr_motion.1D, AFNI, https://afni.nimh.nih.gov/), spatial normalization via subject's T1 image (T1 normalization to MNI space (nonlinear transform), normalization of EPI image to MNI space (3dNWarpApply, AFNI, https://afni.nimh.nih.gov/), interpolation to 2 mm isotropic voxels and smoothing with a 6 mm FWHM kernel (SPM 8, https://www.fil.ion.ucl.ac.uk/spm/software/spm8/).

Prior to first level (within-subject) analysis, we removed the first four volumes to allow for image intensity stabilization. We also identified image-wise outliers by computing both the mean and the standard deviation (across voxels) of intensity values for each image for all slices to remove intermittent gradient and severe motion-related artifacts (spikes) that are present to some degree in all fMRI data.

fMRI data analysis. Data were analyzed using SPM12 (http://www.fil.ion.ucl.ac.uk/spm) and custom MATLAB (The MathWorks, Inc., Natick, MA) code available from the authors' website (http://github.com/canlab/CanlabCore). First-level general linear model (GLM) analyses were conducted in SPM12. The six runs were concatenated for each subject. Boxcar regressors, convolved with the canonical hemodynamic response function, were constructed to model periods for the 10-second stimulation and 4-7 second rating periods. The fixation cross epoch was used as an implicit baseline. A high-pass filter of 0.008 Hz was applied. Nuisance variables included (a) "dummy" regressors coding for each run (intercept for each run); (b) linear drift across time within each run; (c) the six estimated head movement parameters (x, y, z, roll, pitch, and yaw), their mean-centered squares, their derivatives, and squared derivative for each run (total 24 columns); and (d) motion outliers (spikes) identified in the previous step. A "single-trial model" was used to uniquely estimate the response to every stimulus in order to assess functional connectivity.

Functional connectivity analysis. Functional connectivity between the hypothalamus and PAG was estimated using Partial Least Squares (PLS) (Wold et al., 2001) regression, which identifies latent multivariate patterns that maximize the covariance between two blocks of data (i.e., BOLD activity in hypothalamus and PAG voxels). Here, data comprised single trial estimates of brain activation in response to aversive thermal, mechanical, auditory, and visual stimuli, in addition to a set of pleasant visual stimuli which were used as a control. For the PLS model, the predictor block of variables included all voxels in an anatomically defined mask of the hypothalamus (Pauli et al., 2018) (337 voxels) and the outcome block included all voxels in the PAG (Kragel et al., 2019) (42 voxels). Localization of the hypothalamus signal that covaries with the PAG responses was performed by bootstrapping the PLS regression and examining the distribution of PLS regression coefficients and their deviation from zero (using normal approximation for inference). Hyperalignment of fMRI data (Haxby et al., 2011) was

conducted separately for each region as a preprocessing step, and leave-one-subject-out cross-validation was performed to estimate the strength of functional connections (i.e., the Pearson correlation between the first 'X score' and 'Y score' estimated by PLS, similar to the canonical correlation (Hardoon et al., 2004).

A benefit of the pathway-identification model we employed is that it can, in principle, identify HTH and PAG patterns that distinctly participate in the HTH-PAG pathway. For example, the central nucleus of the amygdala (CeA) projects to both the hypothalamus and the PAG (Kim et al., 2013), and could indirectly explain variation in BOLD signals in the PAG. To test pathway specificity, we separately modeled a pathway between the CeA and the PAG using the approach described above. This allowed us to evaluate how much variation in PAG activity the HTH-PAG pathway explained above and beyond the CeA-PAG pathway. To evaluate this, we computed the partial correlation between latent sources in the hypothalamus and PAG, controlling for the latent source in the CeA.

Statistics. Nonparametric Wilcoxon signed-rank or rank-sum tests were used, unless otherwise stated. Two-tailed tests were used throughout with α=0.05. Asterisks in the Figures indicate the *p* values. Standard error of the mean was plotted in each Figure as an estimate of variation. Multiple comparisons were adjusted with the false discovery rate method.

Behavioral cohort information. Initial behavioral characterization of the assays (Figure 1) was replicated 3 times, with cohorts containing 10, 10 and 12 mice (32 in total). PMd cell body fiber photometry experiments (Figure 2) were replicated twice with cohorts containing 7 and 8 mice (15 in total). Miniscope experiments (Figures 3 and 4) were replicated twice, with cohorts of 4 and 5 mice (9 in total). Chemogenetics experiments (Figure 5) were replicated twice (cohort 1 with 10 controls and 6 hM4Di mice and cohort 2 with 9 controls and 5 hM4Di mice). ChR2 experiments (Figure 6) were done once, with 5 YFP and 4ChR2 mice. dlPAG fiber photometry experiments (Figure 7) were replicated twice, with cohorts of 4 and 5 mice (9 in total). Amv body fiber photometry experiments (Figure 7) were replicated once with 6 mice. PMd-dlPAG optogenetic projection inhibition experiments (Figure 8) were replicated twice. Both cohorts had 12 controls and 6 arch mice. PMd-amv optogenetic projection inhibition experiments (Figure 8) were replicated twice. Both cohorts had 6 controls and 9 arch mice. Appropriate fluorophore-only expressing mice were used as controls for chemogenetic and optogenetic experiments. For fMRI data (Figure 9), a cohort of 48 human subjects was used only once. Each mouse was only exposed to each assay once, as defensive behavior assays cannot be repeated. Thus, there are no technical replicates. No outliers were found or excluded. All mice and humans were used. Sample sizes for human and mouse experiments were determined based on comparisons to similar published papers.

For chemogenetic and optogenetic experiments, mice in each cage were randomly allocated to control (mcherry or YFP -expressing mice) or experimental conditions (hM4Di, ChR2 or Arch –expressing mice). Data collection was done blinded to treatment group in mice. For human fMRI data and mouse neural activity recordings, all data were obtained from subjects in identical conditions, and thus they were all allocated to the same experimental group. There were no experimentally controlled differences across these subjects and, thus, there were no "treatment groups".

Data and code availability.

Custom analysis scripts are available at

992 https://github.com/schuettepeter/PMd_escape_vigor.
993 Data is available at
994 https://datadryad.org/stash/share/dYuSl2nnXsyi0nTDjCDeHR08gwW7paFL4Eo3TmF_aH4
995

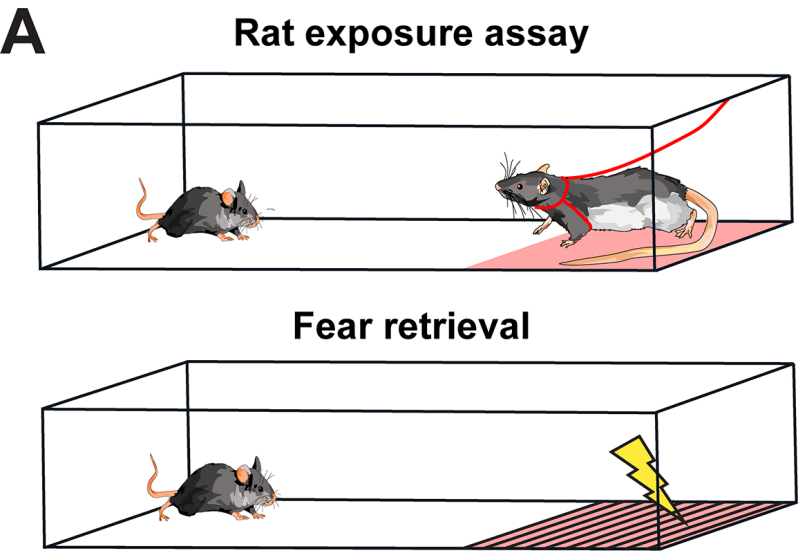

B

Order of Assays (each 10 min.)

1) Toy rat exposure assay
2) Rat exposure assay
3) Pre-shock
4) Fear acquisition
5) Fear retrieval